View metadata, citation and similar papers at core.ac.uk
brought to you by CORE
provided by University of Queensland eSpace

THE UNIVERSITY OF QUEENSLAND
AUSTRALIA

Improved *ab-initio* calculation method for Ge_xSi_{1-x} alloys

Junjie Li
Bachelor of Materials Engineering

A thesis submitted for the degree of Master of Philosophy at
The University of Queensland in 2019

School of Mechanical and Mining Engineering

Abstract

Ge_xSi_{1-x} alloy, a complete solid-solution semiconductor with a diamond structure which contains two face-centred cubic (fcc) sublattices shifted by one quarter along the body diagonal, is one of the most promising material systems in the field of high performance Thermoelectric (TE) materials, having a series of TE applications. Also, due to its excellent potential in energy gap engineering and lattice parameter engineering, Ge_xSi_{1-x} is widely used in preparation of microelectronics, optoelectronic devices and various functional materials, such as making photoconductive detectors and integrated optoelectronic devices.

In this work, several Ge_xSi_{1-x} structure models with certain Ge contents were established, and their mechanic properties and electronic properties were calculated within the Vienna *Ab-initio* Simulation Package (VASP) and discussed. It is investigated that, from x=0 to x=1, Ge_xSi_{1-x} alloy structures are mechanically stable in the cubic phase, their hardness, stiffness, brittleness, band gap width, DOS orbital contribution and bonding nature agree with experimental and theoretical value quite well. Non-linear nature of Ge_xSi_{1-x} alloy band gap value versus Ge content x has proved in this work, the inflection point calculated is quite close to experimental one.

Besides, the common issue verified in this work is that Local Density Approximation and Generalised Gradient Approximation Perdew-Burke-Ernzerhof functionals underestimate semiconductor's band gap value. Hybrid functional HSE06 is found to perform much better on band gap calculation, and the band structures of III-V ternary alloys $In_xGa_{1-x}As$ and $Al_xGa_{1-x}As$ were calculated as well to prove that.

Declaration by author

This thesis is composed of my original work, and contains no material previously published or written by another person except where due reference has been made in the text. I have clearly stated the contribution by others to jointly-authored works that I have included in my thesis.

I have clearly stated the contribution of others to my thesis as a whole, including statistical assistance, survey design, data analysis, significant technical procedures, professional editorial advice, and any other original research work used or reported in my thesis. The content of my thesis is the result of work I have carried out since the commencement of my research higher degree candidature and does not include a substantial part of work that has been submitted to qualify for the award of any other degree or diploma in any university or other tertiary institution. I have clearly stated which parts of my thesis, if any, have been submitted to qualify for another award.

I acknowledge that an electronic copy of my thesis must be lodged with the University Library and, subject to the policy and procedures of The University of Queensland, the thesis be made available for research and study in accordance with the Copyright Act 1968 unless a period of embargo has been approved by the Dean of the Graduate School.

I acknowledge that copyright of all material contained in my thesis resides with the copyright holder(s) of that material. Where appropriate I have obtained copyright permission from the copyright holder to reproduce material in this thesis.

Publications during candidature

No publications.

Publications included in this thesis

No publications included.

Contributions by others to the thesis

Dr Graeme Auchterlonie and Prof Jin Zou have contributed to design of the project and critically revising the thesis.

Statement of parts of the thesis submitted to qualify for the award of another degree

None.

Research Involving Human or Animal Subjects

No animal or human participants were involved in this research.

Acknowledgements

I would like to thank my principle supervisor, Prof Zou Jin, for providing opportunity for me to do the research in his group for 2 years, and his significant help in the design of my project is appreciated as well. At the same time, I would like to thank my secondary supervisor, Dr Graeme Auchterlonie, for his patient guidance during my candidature and great help preparing this thesis. Without these two supervisors, it would be very difficult for me to finish my research project.

I would also like to say thanks to other professor and fellows in Prof Jin Zou's research group: Prof Zhigang Chen, Dr Min Hong, Xiaolei Shi, Han Gao, Weidi Liu, Qiang Sun, Yuzhe Yang, Raza Moshwan, Van Nguyen, Youichirou Kawami, Shengduo Xu, Lijun Wang, Meng Li.

Dr Qinghong Yuan, from Australian Institute for Bioengineering and Nanotechnology, and her group also provided help, thanks to all.

Calculations in this work were supported by the Research Computing Centre at the University of Queensland, which were also acknowledged.

Financial support

No financial support was provided to fund this research.

Keywords

Ge_xSi_{1-x}, *ab-initio*, VASP, elastic, band gap, underestimate, HSE06

Australian and New Zealand Standard Research Classifications (ANZSRC)

ANZSRC code: 091299 Materials Engineering not elsewhere classified, 100%

Fields of Research (FoR) Classification

FoR code: 0912 Materials Engineering, 100%

Content

1 Introduction 1
1.1 Background 1
1.2 Improvements in calculation methods 2
1.3 Objective and scope 3
1.4 Outline 3
2 Literature Review 4
2.1 Ge_xSi_{1-x}: An Excellent Thermoelectric Material 4
2.2 Thermoelectric Materials 6
2.2.1 Thermoelectric Effects 7
2.2.2 Band Gap of Thermoelectric Materials 11
2.2.3 Applications 12
2.3 Ge_xSi_{1-x} 13
2.3.1 Growth method 14
2.3.2 Properties 15
2.3.3 Applications 16
2.4 Summary 20
3 Methodology 21
3.1 Modelling - Materials Studio 21
3.2 *Ab-initio* calculations 26
3.2.1 Density functional theory 26
3.2.2 Exchange functional 26
3.2.3 Computational procedure 27
4 Results and Discussion 29
4.1 Mechanical properties 29
4.1.1 Lattice parameter 29
4.1.2 Elastic properties 29
4.2 Electronic properties 32
4.2.1 Band gap 32
4.2.2 DOS and charge density 36
5 Summary and future work 38

5.1 Conclusion 38
5.2 Limitation 38
5.3 Future work 39
6 Bibliography 40

Table of figures

Figure 1-1 Electricity consumption of the world, 1990~2016[2] 1
Figure 1-2 Electricity consumption of P. R. China, 1990~2016[2] 1
Figure 1-3 Electricity consumption of India, 1990~2016[2] 1
Figure 2-1 Thermal resistivity of $GexSi1-x$ alloys at 300 K[23] 4
Figure 2-2 Thermal conductivity of nanocomposites with 0.8% volume fraction of different nanoparticles. (a) Results at 300 K. (b) Results at 900 K.[29] 5
Figure 2-3 A thermoelectric circuit composed of materials of different Seebeck coefficients[39] 7
Figure 2-4 The Seebeck circuit configured as a thermoelectric cooler[39] 8
Figure 2-5 A thermoelectric generation unit[59] 12
Figure 2-6 GexSi1-x experimental band gap value[10] 15
Figure 2-7 Cassini spacecraft[88] 18
Figure 2-8 Workers were installing GPHS-RTG into Cassini[89] 18
Figure 2-9 Schematic cross-section of SiGe HBT[96] 19
Figure 2-10 Cross-sectional view of FET[97] 20
Figure 3-1 Structural models of GexSi(1-x) alloys with different Ge and Si contents..... 24
Figure 3-2 Structural models of $In_xGa_{1-x}As$ alloys with different InAs and GaAs contents 25
Figure 3-3 Structural models of $Al_xGa_{1-x}As$ alloys with different InAs and GaAs contents 25
Figure 4-1 GexSi(1-x)'s lattice parameter after structual relaxation................................ 29
Figure 4-2 Elastic properties of Ge_xSi_{1-x} alloys 31
Figure 4-3 Ge_xSi_{1-x} band gap calculated by different functionals.................................... 32
Figure 4-4 $In_xGa_{1-x}As$'s band gap calculated by different functionals 34
Figure 4-5 $Al_xGa_{1-x}As$'s band gap calculated by different functionals............................ 35
Figure 4-6 Band structure and pDOS of Ge_1Si_7.. 36
Figure 4-7 Charge density 3D isosurface graph of Ge_4Si_4 37
Figure 4-8 Charge density 2D contour maps of Ge_4Si_4 along (011) plane (a) and Ge_3Si_5 along (111) plane (b).. 37

List of Abbreviations

TE: Thermoelectric

Fcc: Face-centred Cubic

HBT: Heterojunction Bipolar Transistor

FET: Field Effect Transistor

LDA: Local-density Approximation

GGA: Generalized Gradient Approximation

PBE: Perdew-Burke-Ernzerhof

ZT: Figure of Merit

TEG: Thermoelectric Power Generator

TEC: Thermoelectric Cooling Devices

RTG: Radioisotope Thermoelectric Generator

CZ: Czochralski Method

FZ: Floating Zone Method

GSMBE: Gas Source Molecular Beam Epitaxy

SSMBE: Solid Source Molecular Beam Epitaxy

UHV/CVD: Ultra-vacuum Chemical Vapor Deposition

RTCVD: Rapid Heating Chemical Vapor Deposition

GPHS-RTG: General-purpose Heat Source Radioisotope Thermoelectric Generator

ISPM: International Solar Polar Mission

BJT: Bipolar Junction Transistor

CMOS: Complementary Metal-oxide-semiconductor

MOSFET: Metal Oxide Semiconductor Field Effect Transistor

QWIP: Quantum Well Infrared Photodetector

COD: Crystallography Open Database

ICSD: Inorganic Crystal Structure Database

DFT: Density Functional Theory

VASP: Vienna *Ab-initio* Simulation Package

PAW: Projector-augmented Wave

HSE06: Heyd–Scuseria–Ernzerhof-06

1 Introduction

1.1 Background

Over the past several decades, the annual world electricity consumption has increased from 10,000 TWh to around 21,000 TWh[1]. Most of the power generated in the world is derived from fossil fuel resources[2]. In developing Asian nations, such as India and China, electricity consumption has grown rapidly by 5 to 10 times[1] during the time period. In Australia, for example, until 2015, fossil fuel electricity in Australia still accounted for 88% of the total electricity generated[3]. In the process of combustion of fossil fuels, various gases and solid waste are produced, as well as waste heat from power generation

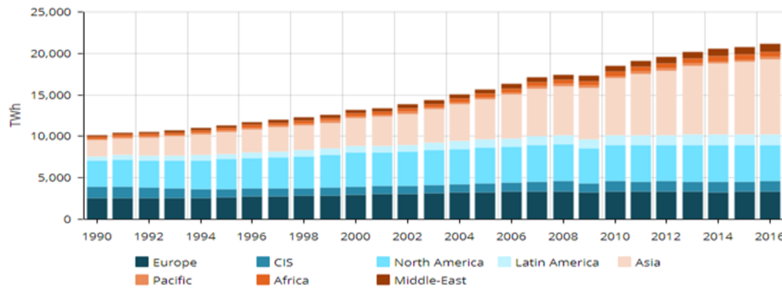

Figure 1-1 Electricity consumption of the world, 1990~2016[1]

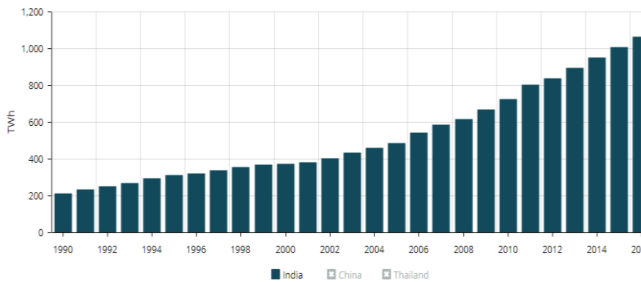

Figure 1-2 Electricity consumption of P. R. China, 1990~2016[1]

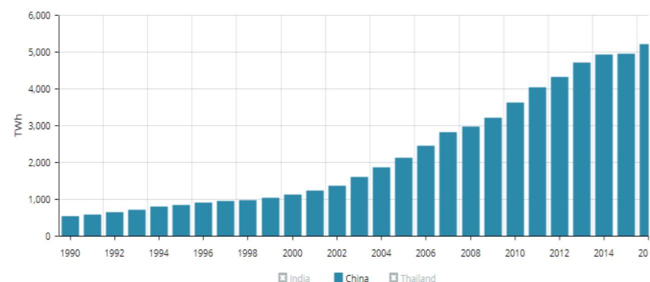

Figure 1-3 Electricity consumption of India, 1990~2016[1]

that all contribute to environmental pollution[4]. There is no doubt that a new revolution of inexpensive, reliable, and low polluting electricity generation is needed to cope with the growing worldwide demand. There are several clean energy technologies being researched and developed at this point in time with thermoelectric (TE) power due to key roles in both primary power generation and energy conservation[5].

Ge_xSi_{1-x} alloys are a complete solid-solution semiconductor suite. All with a diamond structure, which contains two face-centred cubic (fcc) sublattices shifted by one quarter of the lattice parameter along the body diagonal. These alloys are one of the most promising material systems in the field of high performance TE materials[6], showing excellent TE performances at high temperature. Due to their excellent TE performances, these alloys are used in extra-terrestrial missions, serving as the major component of radioisotope thermoelectric generators[7]. Besides, Ge_xSi_{1-x} alloys play important roles in some optoelectrical and electrical devices, including Heterojunction bipolar transistor (HBT)[8] and Field effect transistor (FET)[9]**.**

1.2 Improvements in calculation methods

Band gap is an important property, which is determined by the band structure of semiconductors and related with crystal structures and bond nature. Most valence electrons don't conduct the electric current, which is only conducted when a valence electron bound is promoted to be a conduction electron, the electron is free to move within the crystal lattice and serve as a charge carrier, and the band gap is the minimum energy required to promote. Therefore, the band gap width is a major factor determining the electrical conductivity of the TE materials, by accurately estimating and adjusting the band gap, one can enhance the TE performance of TE materials.

Experimental research across the properties of Ge_xSi_{1-x} series alloy system including band gap has been published in the past[10], and several calculation works have also been performed[11-13]. Most of these calculations are based upon exchange-correlation energy functional approximations, and some of these are the local-density approximation (LDA)[14] and the Generalized Gradient Approximation (GGA)[15] with the Perdew-Burke-Ernzerhof (PBE) form[16]. The LDA and GGA-PBE methods have limited reliability on band gap quantitative prediction, while PBE is more commonly used for calculations of the band gap of Ge_xSi_{1-x} alloys, however, it underestimates the band gap for over 50% of the cases.

To accurately estimate the band gap of Ge_xSi_{1-x} alloy system using *ab-initio* method, and to develop a reliable and repeatable method of semiconductor band gap calculation, an improved *ab-initio* calculation method is required.

1.3 Objective and scope

In this study, Ge_xSi_{1-x} alloys are the major investigated system to be calculated with the Vienna *ab-initio* simulation package (VASP)[17,18], during which, LDA and PBE will be employed to calculate its mechanical and electrical properties, and a new functional will be introduced to specifically calculate the band gap. The band gap data from different methods will be compared and discussed. Other materials' band gap nature will be calculated by the same method to prove the universality of the conclusions.

The purpose of this study is to validate previous Ge_xSi_{1-x} alloy experimental work on its mechanical and electrical properties from the point of view of *ab-initio* calculation, and to improve and summarize the calculation method, so as to draw experience for the future calculation work of other systems.

1.4 Outline

This thesis is divided into five chapters. In addition to this introductory chapter, chapter 2 is a literature review of TE materials and Ge_xSi_{1-x} alloys. The methodology of modelling and computing is in chapter 3, where the fundamentals of *ab-initio* calculations and several different exchange functionals are introduced. The 4th chapter describes the results and discussion of this study, while chapter 5 is the conclusion, with discussions on the limitations of this project, and possible future research directions.

2 Literature Review

2.1 Ge_xSi_{1-x}: An Excellent Thermoelectric Material

Ge_xSi_{1-x} shows excellent TE properties at temperature higher than 600K[19], is an essential member of the TE material family.

The research of Ge_XSi_{1-X}'s TE property started in 1954, when A. V. Ioffe and A. K. Ioffe[20] put up with the view that Ge_xSi_{1-x} alloy can be used as TE materials. They found that the thermal conductivity of Ge_xSi_{1-x} alloy is much lower than pure Si or pure Ge, and carrier mobility has just been affected a little due to the formation of these two matters. This is because that both of Ge and Si has high lattice conductivity (64 W/m K and 145W/m K at 300 K respectively[21]), meanwhile they also have high carrier mobilities, which can yield large value for power factors[22], the value of lattice conductivity of Si falls rapidly when Ge is added, as is shown in Figure 2-1, in which the thermal resistivity is plotted against the Si content in Ge[23]. Therefore, Ge_xSi_{1-x}, the combination of Ge and Si, showing better TE performance than Ge and Si, is an essential member of the TE material family.

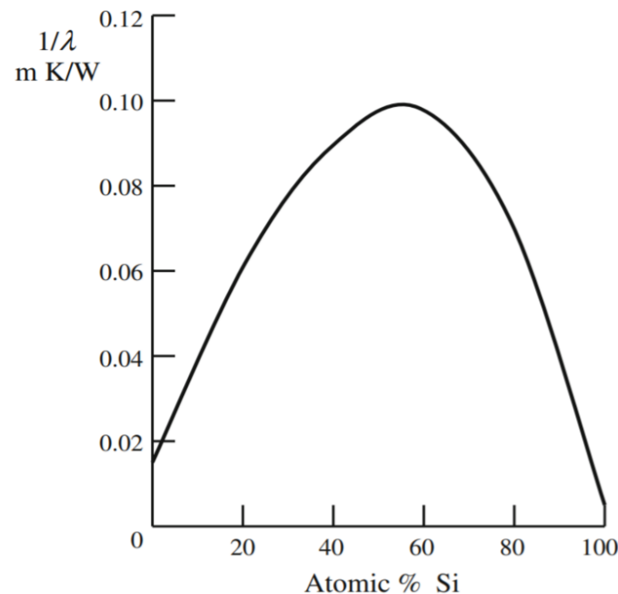

Figure 2-1 Thermal resistivity of Ge_xSi_{1-x} alloys at 300 K[23]

Slack and Moayyed[24,25] have reported in 1991 that the efficiency of Ge_xSi_{1-x} alloy with which the heat converts to electricity in power generation facility is limited by Carnot

efficiency. Consume that thermal conductivity can be decreased to the minimum value, at the same time the electrical conductivity has almost no change, the maximum efficiency can reach to 23.3%.

Compared to bulk material, Ge_xSi_{1-x}'s another form with better TE performance has been obtained by introduction of nanostructure into bulk one, which helps increase the density of nanograin boundaries, so as the phonon scattering, to increases Ge_xSi_{1-x}'s dimensionless figure of merit ZT without weakening its electrical properties.[26]

In 2008, by introducing the nanostructure, Wang et al.[27] have achieved a peak ZT value of around 1.3 at 900 °C in an n-type nanostructured Ge_xSi_{1-x} bulk alloy. In the same year, Joshi et al.[28] used the same approach to study p-type nanostructured Ge_xSi_{1-x} bulk material, then they gained a maximum ZT value of 0.95 at 900 °C.

In 2009, Mingo et al.[29] built 17 different types of silicide nanoparticle models, then they inserted these structures into Ge_xSi_{1-x} bulk material to calculate and compare the influence on TE figure of merit ZT, which is shown in Figure 2-2. They concluded that when 0.8% $NiSi_2$ or Ge nanoparticles volume fraction with 2~10nm particles are introduced into bulk Ge_xSi_{1-x}, the nanocomposite's thermal conductivity can be reduced by 4 to 5 times, a peak ZT value of around 1.7 can be gained at 900 K.

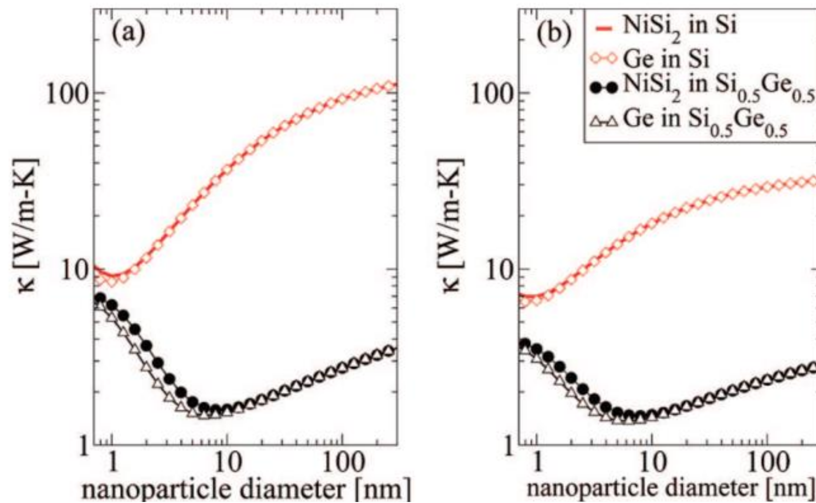

Figure 2-2 Thermal conductivity of nanocomposites with 0.8% volume fraction of different nanoparticles. (a) Results at 300 K. (b) Results at 900 K.[29]

Bera et al.[30] have tried to predict sintered Ge_xSi_{1-x}'s further ZT improvement potential. By comparing their measurement of $Ge_{20}Si_{80}$ and the previous results, they have found

that for n-type material, there would be a 5% enhancement on its TE performance at 1000 K high temperature and a 16% one at room temperature. For p-type $Ge_{20}Si_{80}$, the growth at 1000 K is similar with n-type, for around 4%, and it is 6% at around 300 K. The calculation showed that if phonon scattering by grain boundaries could be made to reach the maximum mismatch degree, the peak ZT value at 1000 K could be more than 2.

In mid-2011, He et al.[31] reported that, by etching nanoscale holes in the $Si_{0.5}Ge_{0.5}$, the material's thermal conductivity can be reduced more than one order of magnitude. It is concluded that less stringent morphological constraints with mass disorder and boundary scattering may reduce the thermal conductivity.

Zhu et al.[32] used Boltzmann transport equation within the relaxation time approximation to calculate several models' TE performances, results showed that both nanostructured Si and Ge_5Si_{95} have lower electrical conductivity and much lower thermal conductivity when compared with their bulk structures. They have achieved an enhancement in figure of merit ZT by a factor of 2 in Nano-Si in comparison with bulk Si. For Ge_5Si_{95} and Nano-Ge_5Si_{95}, their ZT value is 4 times of bulk Si, for about 1.0 at 840 K[33]. They have also compared the impacts from different Ge proportion, found that Ge_5Si_{95} is better than $Ge_{20}Si_{80}$ which are made RTGs by NASA for space projects from last century.

Confinement effect is another feasible approach to decrease thermal conductivity of materials. Some researchers have reported good TE performances of Ge_xSi_{1-x} nanowires. Shi et al. have investigated properties of Ge_xSi_{1-x} nanowires. In their study in 2010, $ZT_{Ge_xSi_{1-x}}/ZT_{Si}$ is a Ge content dependent value. N-type Ge_xSi_{1-x} nanowire has a much better TE performance than its p-type counterpart, and its ZT can be increased by a factor of 4.3 in n-type $Ge_{0.5}Si_{0.5}$ nanowire's. Generally, the experimental ZT value of SiNW is around 0.6-1.0, so they predicted the n-type Ge_xSi_{1-x} nanowire's ZT value should be 2.5-4.0.[34]

2.2 Thermoelectric Materials

TE materials are currently widely investigated all over the world because of their beneficial applications, and Ge_xSi_{1-x} alloys, are a critical member of the TE family, and were selected to investigate the reliably of *ab-initio* calculations of band gap. This chapter discusses the literature review of TE effect fundamentals and their applications.

2.2.1 Thermoelectric Effects

The thermoelectric effect describes a conversion from heat to electricity or vice versa. When a temperature difference occurs on opposite sides of a thermoelectric device, the charge carriers on the hot side will possess more energy. As the result, there should be more hot carriers to diffuse to the cold side than cold carriers that move to hot side, and hence an electric current will flow[35]. Similarly, if a voltage differences exist on a thermoelectric device, there should be different electrical regions at both junctions, and when these charge carriers flow in the device, they will move through different energy levels, and as these level change, they bring about either heat release or absorption, so that a temperature difference occurs.

The thermoelectric effect includes three separate effects: Seebeck effect, Peltier effect and Thomson effect[36-38].

Baltic German Physicist Thomas Johann Seebeck discovered the Seebeck effect in 1821[36] . He found that when different temperatures were applied to the junctions of two dissimilar metals this created a circuit, and compass magnetism could be detected[36], which is shown in Figure 2-3. In the first place, he held the view that the temperature differences directly lead to the magnetism. However, in fact, the magnetism was caused by electric current by Ampere's law. In another words, the heat was converted to electricity, and this phenomenon was defined as Seebeck effect[36].

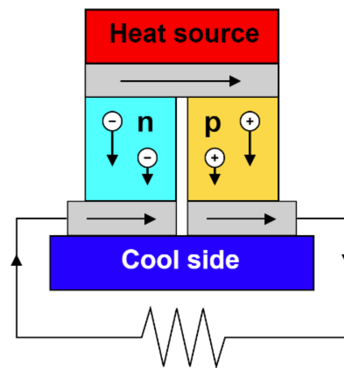

Figure 2-3 A thermoelectric circuit composed of materials of different Seebeck coefficients[39]

In the Seebeck effect, the voltage is proportional to the temperature gradient. The proportionality constant is called Seebeck coefficient S:

$$S = \frac{\Delta V}{\Delta T} \tag{1}$$

where ΔV is the induced voltage, ΔT is the temperature difference.

For general metals, the Seebeck coefficient S could be particularly low, only a few μV/K. However, for semiconductors, this property can reach several hundred μV/K. It can explain why semiconductors are much more promising in thermoelectricity field than metals[40].

Several years later, a French physicist Jean Charles Athanase Peltier found that a voltage current which flows in a circuit of heterogeneous metals can lead to heating or cooling in its junctions[37], which is shown in Figure 2-4. This phenomenon is due largely to the Fermi energy differences between these two different metals. When current passes through a metal or semiconductor, it will change to a different energy level, then the heat flow will be induced[37]. Similarly, with the Seebeck effect, the rate of change of the temperature is proportional to the electrical current produced. The proportionality constant is defined as Peltier coefficient *Π*:

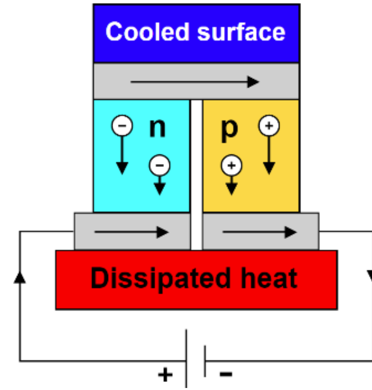

Figure 2-4 The Seebeck circuit configured as a thermoelectric cooler[39]

$$\Pi = \frac{dQ}{dI} \tag{2}$$

where *dQ* is the Peltier heat generated per unit time, *dI* means per unit charge.

In a circuit of metals A & B, there are two unique heat transport mechanisms which share the same electric current but have opposite directions, so when a current I flows in it, the heat absorbed or liberated per unit time *Q* should be:

$$Q = (\Pi_A - \Pi_B) \cdot I \tag{3}$$

In 1856, Scots-Irish mathematical physicist William Thomson used his dynamics theory to comprehensively analyse both the Seebeck and the Peltier coefficients, and found the connecting relationship between them[38]. Previously, no one had successfully proved that Seebeck coefficients have any affinities with Peltier coefficients.

Thomson held the view that there is a simple multiple relation between Seebeck coefficient and Peltier coefficient in absolute 0 K. Based on this view, he theoretically predicted a new thermoelectric effect, that is, when the current flows through the conductor with non-uniform temperature, the conductor will absorb or emit a certain amount of heat in addition to the irreversible Joule heat[38]. Or conversely, when the temperature at both ends of a metal bar is different, it will form a voltage potential difference from one end to another. This phenomenon is called Thomson effect[38], it has become the third thermoelectric effect after the Seebeck effect[36] and the Peltier effect[37].

He predicted the heating or cooling rate per unit volume as:

$$q = -\mathrm{K} \cdot \boldsymbol{J} \cdot \Delta T \tag{4}$$

Where the K is the Thomson effect, J is the density of current which pass through a homogeneous conductor, ΔT is the temperature gradient in the conductor.

The performance of a thermoelectric device is depended on the conductivity of its “internal” components, and the ability of the material to produce thermoelectric power can be measured by the figure of merit ZT:

$$ZT = \frac{\sigma S^2 T}{\mathrm{K}} \tag{5}$$

where σ represents electricity conductivity, S is Seebeck coefficient, T is temperature and K is thermal conductivity[41]. Where ZT is a dimensionless figure of merit.

Generally, power factor is be calculated to measure the work ability of a thermoelectric device, but it doesn’t mean that higher power factor must lead to a higher efficiency. Power factor is defined as:

$$Power\ factor = \sigma S^2 \tag{6}$$

where σ and S is electricity conductivity and Seebeck coefficient respectively.

An actual thermoelectric device should consist of at least two metals, so there should be more than one Seebeck coefficients. Additionally, due to thermoelectric effects, temperature at different part of the device can be dissimilar. Assume a device including two materials, the maximum efficiency η_{max} is:

$$\eta_{max} = \frac{T_H - T_C}{T_H} \frac{\sqrt{1 + Z\bar{\bar{T}}} - 1}{\sqrt{1 + Z\bar{\bar{T}}} + \frac{T_C}{T_H}} \tag{7}$$

where T_H and T_C direct the temperature at the hot and cold junctions respectively.

From the thermoelectric figure of merit ZT’s formula, it can be inferred that there are two keys that decide thermoelectric performance, the power factor and thermal conductivity. In this relationship the power factor is the numerator and the thermal conductivity is the denominator, so increasing the power factor and reducing thermal conductivity are

critical to enhancing the TE performance. There are several ways to achieve better TE properties:

Firstly, preparing certain materials in quantum well superlattice structures have the possibility to significantly increase the Z value, which was published by Hicks and Dresselhause in 1993[42]. Hicks and Dresserhause calculated that Bi_2Te_3 in quantum well structures has the potential to enhance ZT by a factor of 13 over the bulk value if the layer thickness can be as small as 10Å, thus, quantum well multilayer structures may offer another method for improved thermoelectric performance.[42]

Doping is another good way to change a material's electronic band structure, and consequently increase the carrier concentration. Due to enhanced carrier concentration, the density of state near Fermi level increase as well, which can improve the electron transportation between valence band and conduction band.[43,44] Hence, the power factor can be enhanced by doping, and the maximum ZT can be gained when conduction band has a critical distance with Fermi level, where they are close enough and the degeneracy is not very strong.

Additionally, nanomaterials have proven to have much higher ZT value when compared with bulk materials[45]. When the system size decreases to a scale which can compare with its electron mean free path or its wavelength, the quantum confinement effect and energy-filtering effect will have obvious impacts on ZT value enhancement[46]. The density of state will increase, then the Seebeck coefficient will also increase. As the grain size reduces to the nanoscale, the surfaces and interfaces in these nanostructures can significantly scatter the phonons, which reduces the lattice thermal conductivity[47]. However, the scaling of nanomaterials is very difficult, and is still in an exploitative stage of development, and as a result, bulk materials with much lower fabrication costs are the most common commercial thermoelectric materials.[48]

Nanocomposite strategy is another essential means of thermoelectric performance improvement[49]. Introduction of nanoinclusions can be helpful for phonon scattering, and it is very important for high thermal conductivity materials[49]. Nanocomposite strategy has been widely used, and a bunch of materials have been developed based on that, such as half-Heusler alloy, skutterudites, and Si-Ge systems[50-53]. Nanoinclusion strategy is an

easy process and low cost, so it is favourable in both bulk material and nanomaterial areas.

2.2.2 Band Gap of Thermoelectric Materials

The electrical conductivity of a TE material is determined by its carrier concentration and mobility. In order to obtain a larger power factor, the carrier concentration should be within an optimum range, and the carrier mobility must be as high as possible. Typically, the carrier mobility of single crystal is the highest. With the defects in crystal increasing, various carrier dispersions occur, which leads to the decrease of the carrier mobility. As the grain size decreases to nanometre level, the average free path of the carriers will be affected, which will significantly impact on the electrical transport properties of TE materials.

The electrical properties of TE materials are closely related to the bandgap width E_g. The ideal band gap width of TE materials should be around 10 k_BT[54] (k_B is Boltzmann's constant, $k_B = 1.381 \cdot 10^{-23}$ Joules/Kelvin, T is the working temperature). If the band gap width is less than this value, the material will reach the intrinsic excitation state of the semiconductor at a lower temperature. The total Seebeck coefficient is obtained as: $S_{total} = (S_1\sigma_1 + S_2\sigma_2) / (\sigma_1+\sigma_2)$, where 1 and 2 represent electrons and holes respectively[55]. Because the concentration of electrons and holes in the material is equal when the intrinsic excitation occurs, their corresponding electrical conductivity σ_1 and σ_2 have almost the same value. However, the Seebeck coefficient of electrons is negative, while that of holes is positive, so the Seebeck coefficient of the whole system will be drastically reduced[55]. If the band gap is too large, the thermoelectric properties of materials are far from their optimum values at operating temperature.

In fact, $E_g = 10\ k_BT$ is a very ambiguous number, which varies with the carrier concentration and electronic structure characteristics of materials. Since many other physical parameters include doping levels also have an impact on TE properties, it is generally considered that the ideal band gap width for TE materials is about 5-10 k_BT. Therefore, band gap width is a crucial factor affecting material's TE properties. To accurately and efficiently investigate the quantitative relation between band gap and TE performance, an improved band gap *ab-initio* calculation method is needed.

2.2.3 Applications

Among the thermoelectric material applications, the most well-known examples are thermoelectric power generator (TEG) and thermoelectric cooling devices (TEC). Thermoelectric devices are light and small when compared with conventional power generators, and there is no moving parts inside a TE device, so it works silently[56]. Due to that, many remote power generators are developed based on the thermoelectric effect, such as radioisotope thermoelectric generators (RTGs),[57] temperature sensors,[58] and etc. A normal TEG should consist of a large quantity of thermoelectric units, these units are set between two temperature exchanger junctions, which is shown in Figure 2-5. Due to there being no movable part in TEG, it doesn't require service, which means cost saving.[60] Due to their stable structure, TEG have ultra-long life times, and can work under many different and often taxing working conditions[56]. Generation of conventional

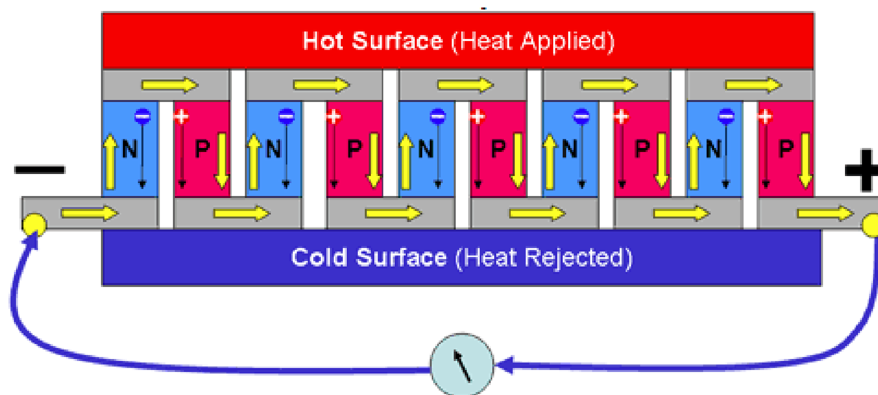

Figure 2-5 A thermoelectric generation unit[59]

electricity is very complex and low-efficiency, because thermal energy must firstly be converted to mechanical energy, then converted into electricity. However, in a TEG, this path is much easier, flowing from thermal energy directly into electricity, as it decreases the waste energy[56]. Based on TEG's feature of long lifespan, it is often used as radioisotope thermoelectric generator (RTG) for energy supply for space projects[61]. An RTG uses an array of thermocouple to convert the heat released by decay of radioactive material into electricity, so it is often used for Satellites and Unmanned remote facilities.

TEC is widely used in thermoelectric air conditioners and thermoelectric refrigerators[62]. Thermoelectric air conditioners are quiet when operating and easy to install, and their working environment can be flexible, and the only reason that thermoelectric air conditioners have not been widely accepted are their high manufacturing cost[63]. As for thermoelectric refrigerators, they can decrease temperature much faster than conventional refrigerators. As well, unlike conventional refrigerators, they work without any noise. Since they have no moving mechanical parts, they can be made portable, which is good for outdoor activities.

Temperature measurement and control is another application field of thermoelectric effect, one example being a thermocouple[64]. It is a temperature sensor that has been widely used, has also been used to convert temperature differences to electrical potential differences. They are inexpensive to manufacture, easy to replace, and have a standard interface, and can be used across large temperature ranges. The main limitation is the precision, and the system error of less than 1 degrees Celsius is usually difficult to reach[65].

The thermocouple is usually connected in series, or sometimes in parallel. Such device consisting of hundreds of thermocouples is defined as a thermopile. A thermopile does not measure the absolute temperature, but it can output a voltage that is proportional to the temperature difference or temperature gradient[66]. For the same temperature difference, the electromotive force in the thermopile is much larger than that of the single thermocouple, and the thermocouple thermometer made by it is more sensitive.

All thermoelectric temperature measurement and control devices have desirable features, such as stable performance, high sensitivity and maintenance free[67] and they do not need an external power supply. When the heat source is adequate and stable, they can take into account both power generation and temperature induction control.

2.3 Ge_xSi_{1-x}

As the investigated material system in this work, Ge_xSi_{1-x} alloys are reviewed in this part, including its properties, experimentally growth method and applications.

2.3.1 Growth method

There are many ways to prepare uniform Ge_xSi_{1-x} crystals, including Czochralski method, Floating Zone method and Bridgman method. In the preparation of Ge_xSi_{1-x} crystals by these methods, very low growth rate (down to around 1mm/h) is required, because there is a large gap between the liquidus and solidus curves in the phase diagram of Ge_xSi_{1-x} alloys, and excessive growth rate will lead to occurrence of constitutional supercooling[68]. The Czochralski (CZ) method is mainly used to grow large Ge_xSi_{1-x} single crystals. In 1999, Yonenage et al. used this method to grow full single crystals of Ge_xSi_{1-x} with $x < 0.15$ and $x > 0.85$, with diameters exceeding 25 mm[69]. Crystals with intermediate composition changed to polycrystalline due to the constitutional supercooling in that work. The advantage of CZ method is that it produces stable crystals, but impurity pollution may occur. The greatest advantage of the Floating Zone (FZ) method lies in the large temperature gradient at the solid-liquid interface, the rapid mixing of melts and the non-pollution of crucibles, so that high quality crystals can be grown. Because the melt is relatively stable, Ge_xSi_{1-x} crystals with high Si content can be produced by this method[68]. In 1996, Wollweberet et al. used this method to produce Ge_xSi_{1-x} crystals with almost no dislocation between 0 and 0.05[70].

Directional Solidification method (Bridgman method) can be used for very small melt. Samples made by this method are suitable for basic research of alloy solid solution[71]. Its growth direction is determined by self-seeding. In this way, Dahlen et al. grew small Ge_xSi_{1-x} single crystals with $x > 0.6$ in 1994[72]. In 1997, Kadokura et al. also applied liquid-encapsulated Bridgman and zone levelling methods to grow Ge_xSi_{1-x} with Ge content from 0.6 to 1.0[73]. The reason for using the zone levelling method is that their strong segregation makes crystal growth non-uniform. Kadokura et al. also confirmed that $CaCl_2$, which flows between the silica ampoule and the Ge_xSi_{1-x} melt for temperatures above 800°C, is the best encapsulant to effectively prevent melt from reacting with crucible.

The research of Ge_xSi_{1-x} alloy materials began in the mid-1950s[68]. It is difficult to improve the quality of materials due to technological reasons. With the development of thin film growth technology, a variety of SiGe/Si structures with good lattice quality and electro-optic properties can be grown. SiGe/Si structures can be grown by a variety of

epitaxy methods. Recent reports mainly focus on gas source molecular beam epitaxy (GSMBE)[74], solid source molecular beam epitaxy (SSMBE)[75], ultra-vacuum chemical vapor deposition (UHV/CVD)[76] and rapid heating chemical vapor deposition (RTCVD)[77].

2.3.2 Properties

Ge_xSi_{1-x} alloys form a complete solid-solution semiconductor series with each alloy having a diamond structure which contains two face-centred cubic (fcc) sublattices shifted by one quarter along the body diagonal. There are three forms of Ge-Si alloys: amorphous, crystalline and superlattice[78]. Amorphous Ge-Si solid solution is mainly used for solar cells[79], and its conversion efficiency has reached more than 10%. The crystalline subgroup includes single crystal and polycrystalline, it's mainly used as TE materials, infrared and nuclear radiation detector materials. Ge-Si alloys have features of high efficiency, high strength, good thermal stability, radiation resistance and are light weighted, which is be widely applied in thermoelectric generators of space systems[80]. Ge_xSi_{1-x} superlattices are new materials with a periodic array consisting of two different semiconductor thin layers arranged alternately. It is obtained by the layer by layer growth of two different semiconductor material thin films on the crystal substrate[81].
The lattice parameters of Ge and Si differ by 4%, and that their alloys form a solid-solution that strictly follows Vegard's Law from 0.534 nm for pure Si to 0.566nm for pure Ge at 300k, while the energy gap changes from 1.16 eV (Si) to 0.72 eV (Ge) with

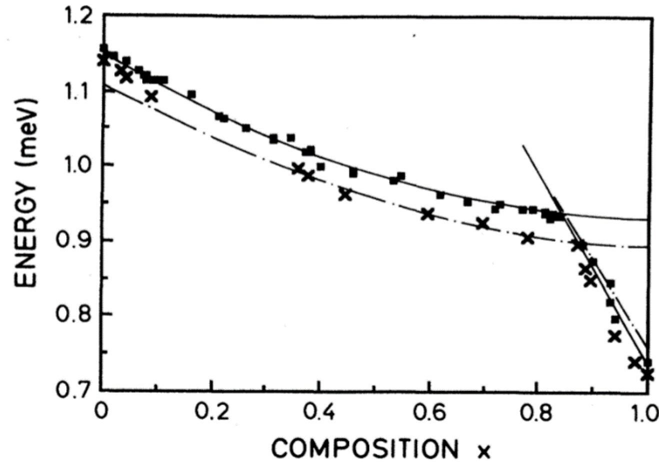

Figure 2-6 GexSi1-x experimental band gap value[10]

the Ge composition increasing. In 1989, Weber et al. applied Photoluminescence (PL) spectra methods to obtain low temperature Ge_xSi_{1-x} alloys' experimental indirect band gap values, which is shown at Figure 2-6. Based on these experimental results, T. P. Pearsall and K. Eberl etc. gave analytical expressions for GeSi band gap[82]:

$$E_{gx}^{(X)}(x) = 1.155 - 0.43x + 0.206x^2 \qquad x \in (0, 0.85) \qquad (8)$$

$$E_{gx}^{(L)}(x) = 2.010 - 1.270x \qquad x \in (0.85, 1) \qquad (9)$$

Due to Ge_xSi_{1-x} alloys having a potential in energy gap engineering and lattice parameter engineering, they have wide application in preparation of microelectronics, optoelectronic devices and various functional materials, such as making photoconductive detectors and integrated optoelectronic devices[83].

2.3.3 Applications

2.3.3.1 Thermoelectric Applications

Ge_XSi_{1-X}, shows excellent thermoelectric performance at high temperature[84]. Its lattice structure leads to heavier phonon scattering effects but almost no influence on electrical conductivity. As a result, Ge_XSi_{1-X} has good thermoelectric properties at high temperature, especially in extra-terrestrial missions, where it plays a critical role.[85]

In extra-terrestrial missions including space missions, Ge_XSi_{1-X} is widely used as the major material of radioisotope thermoelectric generators. Radioisotope thermoelectric generator is essentially a nuclear battery that reliably converts heat into electricity.[86] It works to provide adequate electricity for unmanned remote space and diving facilities. It uses an array of thermocouple to convert the heat released by decay of radioactive material into electricity. Because the radioactive materials are pretty highly efficient, the radioisotope thermoelectric generator's lifetime is extensive, which can ensure these extra-terrestrial facilities are durable, maintenance free and can work for extended period. Besides, due to the good thermoelectric performance of Ge_XSi_{1-X} at high temperature, the volume of a radioisotope thermoelectric generator can be relatively small, which is essential for rocket launched equipment where it will not negatively affect the facility's weight and size. In a radioisotope thermoelectric generator, there are two major components, heat source and energy conversion system. Heat is produced by spontaneous decay of radionuclides. Dissimilar with nuclear fission in reactor system,

radioisotope energy is much safer and run at a lower cost[7]. It is obvious in Table 1 that from 1961 on, NASA has launched more than 30 space missions, they have different names, objectives and destinations, some of them failed and some of them succeeded, but

Table 1 US current and future space missions using RTGs68,69[7,87]

Power source	#RTGs	Spacecraft	Mission type	Launch
SNAP-3	1	Transit 4A	Navigational	1961
SNAP-3	1	Transit 4B	Navigational	1961
SNAP-9A	1	Transit 5BN-1	Navigational	1963
SNAP-9A	1	Transit 5BN-2	Navigational	1963
SNAP-9A	1	Transit 5BN-3	Navigational	1964
SNAP-10A	Reactor	Snapshot	Experimental	1965
SNAP-19	2	Nimbus B-1	Meteorological	1968
SNAP-19	2	Nimbus III	Meteorological	1969
ALRHU	Heater	Apollo 11	Lunar	1969
SNAP-27	1	Apollo 12	Lunar/ALSEP	1969
SNAP-27	1	Apollo 13	Lunar/ALSEP	1970
SNAP-27	1	Apollo 14	Lunar/ALSEP	1971
SNAP-27	1	Apollo 15	Lunar/ALSEP	1971
SNAP-19	4	Pioneer 10	Planetary	1972
SNAP-27	1	Apollo 16	Lunar/ALSEP	1972
Transit-RTG	1	Traid-01-1X	Navigational	1972
SNAP-27	1	Apollo 17	Lunar/ALSEP	1972
SNAP-19	4	Pioneer 11	Planetary	1973
SNAP-19	2 ea.	Viking 1,2	Mars landers	1975
MHW-RTG	2 ea.	LES 8, LES 9	Communication	1976
MHW-RTG	3 ea.	Voyager 1, 2	Planetary	1977
GPHS-RTG	2	Galileo	Planetary	1987
GPHS-RTG	1	Ulysses	Planetary	1990
LWRHU	Heater	Mars pathfinder	Mars rovers	1996
GPHS-RTG	2	Cassini	Planetary	1997
LWRHU	Heater	MER	Mars rovers	2003
GPHS-RTG	1	New horizons	Planetary	2006
MMRTG	1	Curiosity Rover	Mars rovers	2011
MMRTG	-	MSL	Mars rovers	Future
eMMRTG	-	Europa	New frontiers	Future

the common point beyond them is that their power is all from RTGs (radioisotope thermoelectric generators). Material selection for thermal couples is a key part of RTG investigation, excellent thermoelectric performance at high temperature, good stability and light scale are preferred properties for energy conversion system. In this case, Ge_XSi_{1-X} is an excellent candidate material system for RTG preparations.

General-purpose heat source radioisotope thermoelectric generator (GPHS-RTG) is one of Ge_XSi_{1-X}'s applications. GPHS-RTG has ever been the most successful spacecraft power source in the world. Originally, it is conceived to power what was then the International Solar Polar Mission (ISPM; later the Ulysses mission).[87] However, the real first time of GPHS-RTG serving a spacecraft is in Galileo mission in 1987. The GPHS-

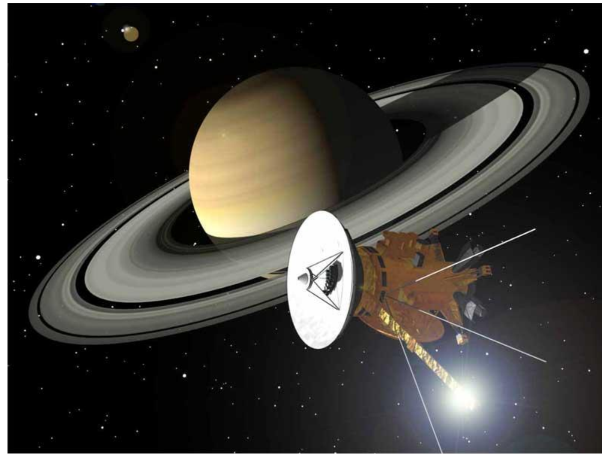

Figure 2-7 Cassini spacecraft[88]

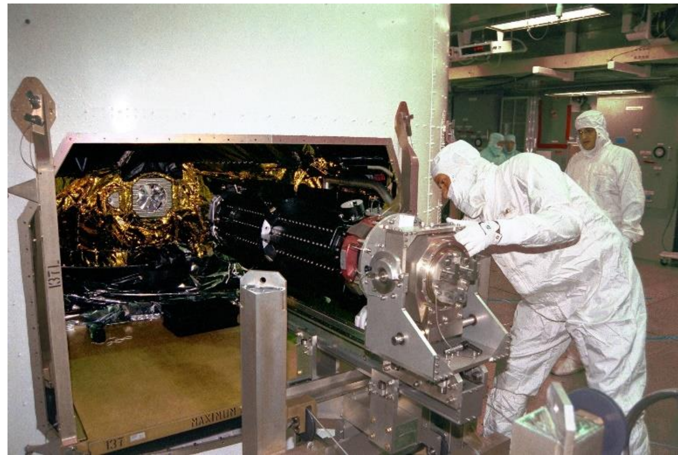

Figure 2-8 Workers were installing GPHS-RTG into Cassini[89]

RTG had powered Galileo for more than 14 years until 2003, when Galileo deliberately crashed into Jupiter at over 48 kilometers per second at its end of life. In 1990, GPHS-RTG powered Ulysses mission launched, after working for 19 year, it stopped communication with controllers and shut down in 2009[90,91]. Cassini mission, which is shown in Figure 2-7, launched in 1997. In September 2017, it crashed into Saturn and

retired. There are 3 GPHS-RTGs in Cassini, Figure 2-8 shows the workers were installing the RTG into Cassini.

2.3.3.2 Optoelectronic Applications

Ge_XSi_{1-X} is widely investigated in optoelectronic application areas.
Heterojunction bipolar transistor (HBT) is a bipolar junction transistor that uses different semiconductor materials for the emitter and base regions, creating a heterojunction structure[92]. It is frequently used for high-speed and high-frequency applications[93]. Generally, III-V compound semiconductors are thought to be an excellent material series for HBT research[94]. GeSi HBT are able to attain comparable performance to III-V compounds, high integration levels, high yield, and low cost[95]. GeSi HBT have been used as components of power amplifiers in mobile phones and laser drivers[8]. Its cross-sectional view is shown in Figure 2-9.

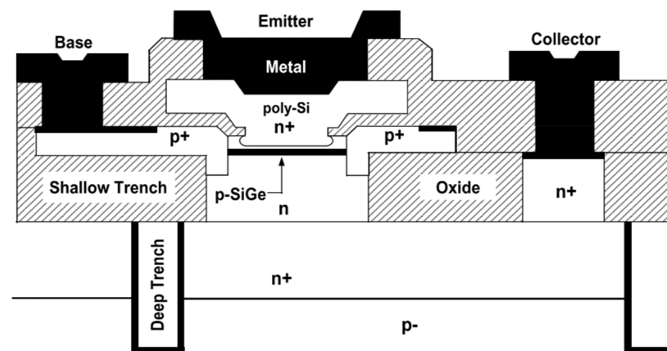

Figure 2-9 Schematic cross-section of SiGe HBT[96]

Compared to conventional bipolar junction transistor (BJT), HBT's emitter and base regions are made from different materials, this design can stop holes injecting from base to emitter, because of the higher barrier potential in valence band than conduction band. So when it is used for digital and analog microwave applications, it can handle the signal with ultrahigh frequencies up to hundreds Giga Hertz.
Based on that, it has many applications, including Power amplifiers in mobile phones and laser drivers.

2.3.3.3 Electronic Applications

Ge_XSi_{1-X} is a good candidate for high power semiconductor devices. Field effect transistor (FET) is one of them. It uses an electric field to control the electrical behaviour

of the device. As shown in Figure 2-10, major components of a FET are source, drain, gate and body, normally the electrons flow between source and drain in body, the

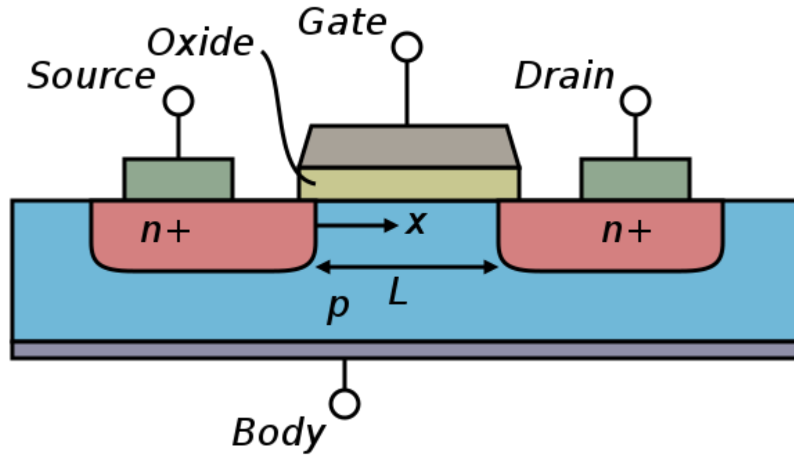

Figure 2-10 Cross-sectional view of FET[97]

particles' transportation is below the gate, so when putting certain electric potential at gate area, the particle transport will be influenced, in a another word, the electrical work of FET can be controlled.

FET field consists of a wide range of practical applications, one of the most famous one is complementary metal-oxide-semiconductor (CMOS). Just as its name implies, CMOS use complementary pairs of p-type and n-type metal oxide semiconductor field effect transistors (MOSFETs) for logic functions.

CMOS is famous for its widely use as image sensor in digital SLRs, which plays a most key role. It is also an important component of computation facilities. With computation industry moving ahead, the requirement of lighter and faster digital integrated circuits continuously makes CMOS smaller and more efficient in recent years[98].

Additionally, in optoelectronic fired, Ge_XSi_{1-X} has much potential. Due to quantum wells in Ge_XSi_{1-X} related heterostructure, many applications have been developed such as quantum well infrared photodetector (QWIP) and resonant tunnelling diode, more details about quantum wells will be given below.

2.4 Summary

Since Ge_xSi_{1-x} is an excellent TE material, this literature review begins with the study of TE materials. Literatures[36-53, 56-67] are selected to help study the fundament and the

applications of TE materials, and to understand the importance of TE performance enhancement. Meanwhile, it is revealed by literatures[54-55] that band structure has a significant influence on the performance of TE materials, and the TE performance can be indirectly controlled by adjusting the band gap. In 2.3, the growth method, properties and applications of Ge_xSi_{1-x} have been discussed. The forms of single crystal and superlattices of Ge_xSi_{1-x} are introduced by the literatures[78-83]. Ge_xSi_{1-x}'s experimental bandgap data in literature[10] also provides good comparison for the calculation of this study, which can be used to test the accuracy of calculation results.

When comparing the experimental data[10] and calculation data[11-13], tt can be observed that conventional GGA-PBE and LDA methods often incur errors when calculating the band gap of Ge_xSi_{1-x}. Therefore, another *ab-initio* band gap calculation method for Ge_xSi_{1-x} is needed.

3 Methodology

The major steps of this project are modelling, calculation and analysis. In this order, descriptions of corresponding methods are stated below.

3.1 Modelling - Materials Studio

Developed by Accelrys®, Materials Studio is a world leading materials software which possesses some of the world's most advanced materials simulation methods and modelling technologies.[99] Materials Studio consists of a suite of programs including CASTEP, ONETEP, DMol3, VAMP, etc., and is generally accepted as being reliable for calculation in computational chemistry, bioinformatics, cheminformatics, molecular dynamics simulation, quantum mechanics, etc..[100] In this project, Materials Studio is used for crystal structure construction.

To build a viable and appropriate crystal structure model, for example Ge_1Si_3, normally there are three methods of choice:

1. To directly look for a crystallographic structure file for Ge_1Si_3 in databases such as Acta Crystallographica, Crystallography Open Database (COD) and software Inorganic Crystal Structure Database (ICSD). If the structures are listed, they can be either experimental or theoretical, and their veracity accessed. The major

weakness of these databases is that mainly bulk structures have been determined, with limited nano-sized structures listed. In this case, bulk Ge_1Si_3 structure was not found.

2. To directly build the crystal structure. Some parameters about the structure to be built are needed: lattice parameters (a, b, c, α, β, γ), space group (space group number preferred) of this structure and exact atomic position of unit cell (x,y,z and atom type).[99] Generally, this construction method relies on accurately determined lattice parameters, especially for complex crystal structures, so that it is easy to make mistakes in forming the precise structure.
3. To use Materials Studio to modify a standard model that is from the database or BIOVIA™ Materials Studio structure base. In this case, there is no existing Ge_1Si_3 crystal structure, so a model structure is required, and was generated by modifying a known Ge_XSi_{1-X} structure.
   Si forms into the diamond structure where its conventional unit cell consists of 8 Si atoms. Replacing 2 of these Si atoms with Ge atoms attains the Ge_1Si_3 structure. All possibilities for $0 < x < 1$ in 0.1 steps have been calculated. Lattice parameters for known alloy concentrations were obtained from previous experiment work[6], while those structures with specific Ge-Si ratios, were interpolated using Vegard's Law[101] to predict the band gap from neighbouring experimental values.
   Based on Vegard's law, the lattice parameter of Ge_xSi_{1-x} is approximately equal to a rule of mixtures of the Ge and Si's lattice parameters at the same temperature, shown as:

$$\alpha_{\mathrm{GexSi(1-x)}} = x\alpha_{Ge} + (1-x)\alpha_{Si} \quad (10)$$

   where x indicates the Ge content in Ge_xSi_{1-x}; $\alpha_{\mathrm{GexSi(1-x)}}$, α_{Ge} and α_{Si} are the lattice parameters of Ge_xSi_{1-x}, pure Ge and pure Si.

Based on the 3rd method, nine structural models were established– Si, Ge_1Si_7, Ge_1Si_3, Ge_3Si_5, Ge_1Si_1, Ge_5Si_3, Ge_3Si_1, Ge_7Si_1 and Ge, as Figure 3-1. Both lattices of pure Si and pure Ge are Fd-3m:1 space group with lattice parameter (a_o) of 5.4307**Å** and 5.6574**Å** respectively at T=300k[102]. So, the lattice parameters of Ge_xSi_{1-x}'s lattice parameters are linearly distributed between 5.4307**Å** and 5.6574**Å.**

To help support a viewpoint for this methodology, ten structural models of III-V ternary alloys $In_xGa_{1-x}As$ and $Al_xGa_{1-x}As$ were established, as shown in Figure 3-2 and Figure 3-3 respectively. Their unit cell formations belong to the same Space group as that of the Ge_xSi_{1-x} binary alloy suite. For each chemical variation in the alloy suite, atom substitution was performed, for example, $In_{0.25}Ga_{0.75}As$, replacing 1 of 4 Ga atoms with In atom attains the target structure. Based on Vegard's Law, structures' lattice constants were estimated by:

$$\alpha_{\mathrm{In}_x\mathrm{Ga}_{1-x}\mathrm{As}} = x\alpha_{InAs} + (1-x)\alpha_{GaAs} \qquad (11)$$

$$\alpha_{\mathrm{Al}_x\mathrm{Ga}_{1-x}\mathrm{As}} = x\alpha_{AlAs} + (1-x)\alpha_{GaAs} \qquad (12)$$

where x indicates the InAs content in $In_xGa_{1-x}As$ and the AlAs content in $Al_xGa_{1-x}As$; $\alpha_{\mathrm{In}_x\mathrm{Ga}_{1-x}\mathrm{As}}$, α_{InAs}, α_{GaAs}, $\alpha_{\mathrm{Al}_x\mathrm{Ga}_{1-x}\mathrm{As}}$ and α_{AlAs} are the lattice parameters of $In_xGa_{1-x}As$, pure InAs, pure GaAs, pure $Al_xGa_{1-x}As$ and pure AlAs, respectively. $In_1Ga_3As_4$, $In_2Ga_2As_4$, $In_3Ga_1As_4$, $Al_1Ga_3As_4$, $Al_2Ga_2As_4$ and $Al_3Ga_1As_4$'s lattice constants are predicted as 5.7546**Å**, 5.8558**Å**, 5.9570**Å**, 5.6553**Å**, 5.6573**Å** and 5.6594**Å**, respectively.

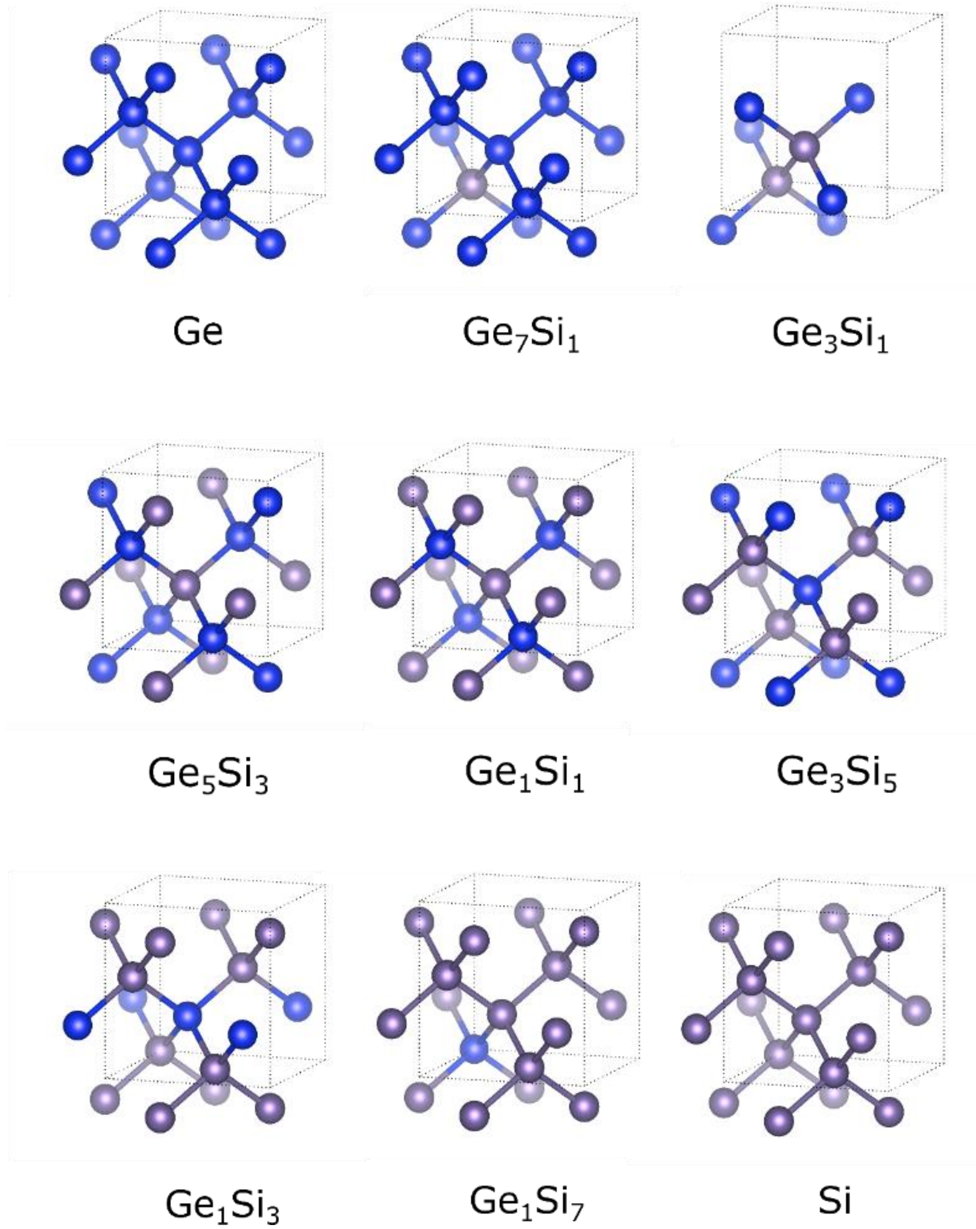

Figure 3-1 Structural models of GexSi(1-x) alloys with different Ge and Si contents

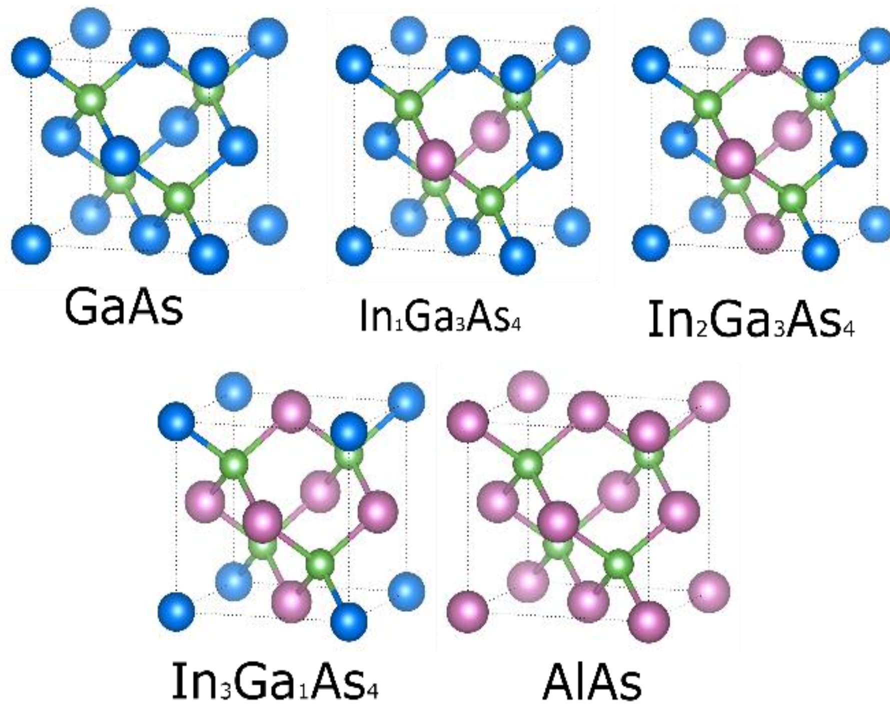

Figure 3-3 Structural models of $In_xGa_{1-x}As$ alloys with different InAs and GaAs contents

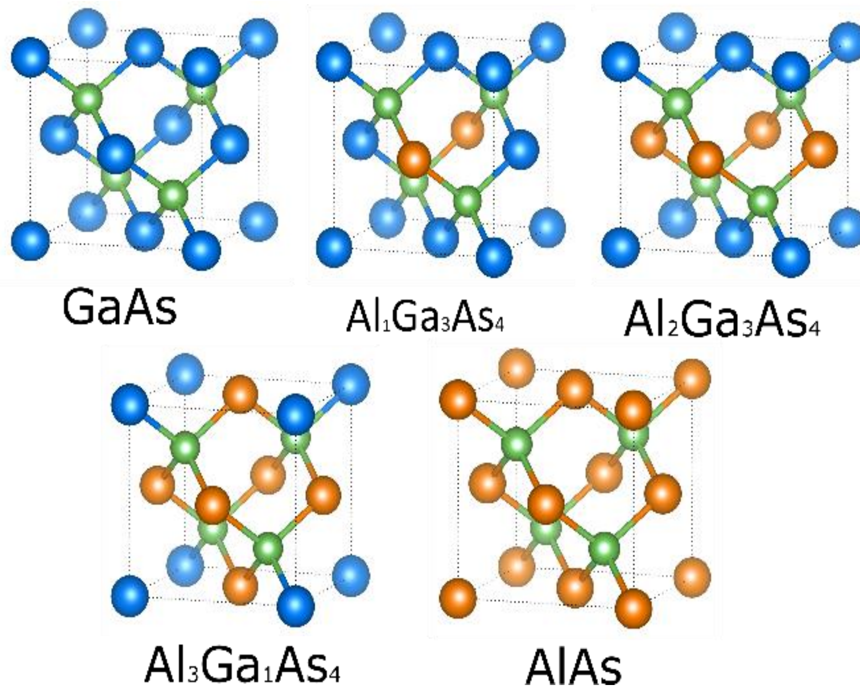

Figure 3-2 Structural models of $Al_xGa_{1-x}As$ alloys with different InAs and GaAs contents

3.2 *Ab-initio* calculations

Based on Density Functional (DFT) Theory, *ab-initio* calculations were performed using the Vienna *ab-initio* simulation package (VASP)[17,18], a sophisticated package for calculating *ab-initio* quantum-mechanical molecular dynamics simulations. It uses either pseudopotentials or projector-augmented wave (PAW) method and a plane wave basis set to calculate forces and the full stress tensors so that atoms can be relaxed into their instantaneous ground-state[103,104].

3.2.1 Density functional theory

Originally, in the calculation of the many-body structure, the nucleus is regarded as stationary (Born-Oppenheimer approximation)[105], so that electrons can be regarded as moving in the electrostatic potential *V* generated by the nucleus. States of electrons can be described by Schrödinger equation:

$$H\Psi = [T + V + U]\Psi = \left[\sum_{i}^{N} -\frac{\hbar^2}{2m}\nabla_i^2 + \sum_{i}^{N} V(\vec{r_i}) + \sum_{i<j} U(\vec{r_i}, \vec{r_j})\right]\Psi = E\Psi \quad (13)$$

Where *N* is the electron number, *U* is the interaction potential of the electron. The operators *T* and *U* are pervasive operators, which are the same in all systems, while the operator V is dependent on the system and is not universality. However, solution of Schrödinger equation needs too much work, which is not suitable for complex systems. In contrast, the density functional theory transforms the many-body problem with U into a single-body problem without U. The electron density $n(\vec{r})$ is given by:

$$n(\vec{r}) = N\int d^3\, r_2 \int d^3\, r_3 \dots \int d^3\, r_N \Psi^*(\vec{r_1}, \vec{r_2}, \vec{r_3}, \dots, \vec{r_N})\Psi(\vec{r_1}, \vec{r_2}, \vec{r_3}, \dots, \vec{r_N}) \quad (14)$$

Currently, the most successful DFT was developed by Kohn and Sham, which brought the Nobel prize to Kohn in 1998.[106-108]

3.2.2 Exchange functional

Kohn-Sham density functional theory is widely used to calculate the properties of atoms, molecules[14], and solids' ground-state using a self-consistent-field[109]. The major challenge of this theory is that the exchange-correlation energy:

$$E_{XC} = E_X + E_C \quad (15)$$

must be approximated. The simplest approximation is a local-density approximation (LDA)[14], which can be gained from Thomas-Fermi model[110,111]. It depends solely upon the value of the electronic density at each point in space, which is represented as:

$$E_{xc}^{LDA}[\rho] = \int \rho(\boldsymbol{r})\, \varepsilon(\rho) d\boldsymbol{r} \tag{16}$$

where ρ is the electronic density and ε_{xc} is the exchange-correlation energy per particle of a homogeneous electron gas of charge density ρ.

Generalized Gradient Approximation (GGA)[15] brings an improvement in the accuracy provided by the LDA. LDA focuses the density value at a certain point. However, GGA takes its gradient into account, where the Perdew-Burke-Ernzerhof (PBE) functional is a form of GGA functionals[16], which contains experimental parameters whose values have been fitted to reproduce experiment or more accurate calculations.

Both LDA and GGA-PBE have been employed in the structural and elastic properties section to compare with experimental values. In bandgap calculations, it was found that, hybrid functional obtained more accurate results.[112-115] Heyd–Scuseria–Ernzerhof-06 (HSE06)[116] hybrid functional is modified from the conventional GGA-PBE. The difference between them is that HSE06 replaces the previous exchange energy in PBE with a new one mixed Hartree-Fock and PBE's exchange energy for a certain range:

$$E_X^{HSE} = \alpha E_X^{HF,SR}(\mu) + (1-\alpha) E_X^{PBE,SR}(\mu) + E_X^{PBE,LR}(\mu) \tag{17}$$

Where α is the mixing parameter between short-range HF exchange energy $E_X^{HF,SR}(\mu)$ and the short-range PBE energy $E_X^{PBE,SR}(\mu)$, usually α = 0.25; μ controls the screening, which can define the range of HF correction, normally μ = 0.2 $Å^{-1}$ in HSE06 functional.

3.2.3 Computational procedure

Before precise calculations were performed, internal coordinates of the perturbed structures were relaxed. A conjugate-gradient algorithm is used to relax the ions into their instantaneous ground state. The cut-off energy of the plane wave basis was set at 450eV to keep calculations both accurate and efficient. Using a Gaussian smearing method[117], the smearing width was set to 0.2eV. To make the relaxed structure resemble the experimental one, only ions and cell volume were changed to maintain crystal shape.

After the relaxation, the structure turns to a steady state that is of low energy. This is followed the self-consist calculation. This calculation aims to improve the structural model to obtain the lowest system energy by forcing strict wave function and charge density values. Accurate Fermi level location can be computed in the self-consist calculation and based on this result, the crystal's electronic structure, such as band gap and density of state, can be further calculated with realistic expectations.

4 Results and Discussion

4.1 Mechanical properties

4.1.1 Lattice parameter

Structural optimization is an essential procedure in *ab-initio* calculations. In this study, the PBE and LDA method were employed to relax the lattice constants of modeled structures, and the results are listed in Table 2 and Figure 4-1.

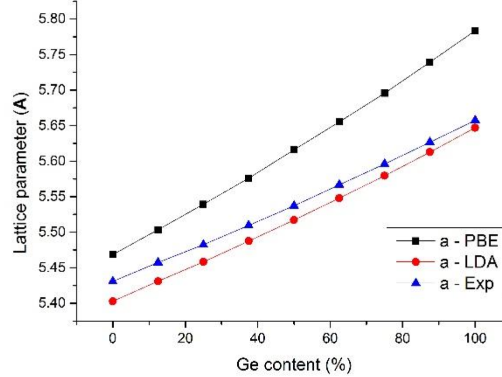

Figure 4-1 GexSi(1-x)'s lattice parameter after structual

It was found that, compared with previous experimental values[10], the constant *a* calculated by PBE is slightly larger for Si-like compositions, while the band gap increases with increased Ge content. However, it should be noted that LDA figures are always lower than the experimental one[10]. The gap gradually decreases to quite small values with structure tending to be more Ge-like.

Table 2 Ge_xSi_{1-x}'s experimental and structural relaxed lattice parameters

	Si	Ge_1Si_7	Ge_1Si_3	Ge_3Si_5	Ge_1Si_1	Ge_5Si_3	Ge_3Si_1	Ge_7Si_1	Ge
PBE	5.468	5.504	5.539	5.576	5.616	5.655	5.696	5.739	5.783
LDA	5.403	5.431	5.458	5.487	5.517	5.548	5.580	5.613	5.647
EXP	5.431	5.457	5.483	5.509	5.537	5.567	5.596	5.627	5.658

4.1.2 Elastic properties

To understand the elastic properties of the GeSi alloy system, calculations were performed for the values of three independent second-order elastic constants (C_{ij}) using first-principle calculations based on "stress-strain" method, data is shown at Figure 4-2 and Table 3 below. For the cubic phase, the stability condition is $C_{11} > 0$, $C_{44} > 0$, $C_{11} > C_{12}$, $C_{11} + 2C_{11} > 0$, $C_{12} < B < C_{11}$[118,119]. In this study, the elastic constants of all structures meet the condition, which demonstrates that the structures are mechanical stable in the cubic phase. These elastic constants were calculated by PBE and LDA method, most of

the PBE values are slightly greater than the LDA. When a linear compression is applied to the material along the x-direction, the larger the value of C_{11}, the more resistive the material is to the greater applied external force[120]. Pure Si shows greater incompressibility along the x-direction than pure Ge, and because of that, GeSi alloy system exhibits a linearly increasing compressibility with increasing Ge content. Similarly, C_{44} represents the resistance to shear deformation concerning applied shear stress across the (100) plane along the z-axis, which indirectly measures the hardness of a material, so it can be understood that less Ge content in GeSi alloy system leads to harder

Table 3 Elastic parameters of Ge_xSi_{1-x} alloys

Si	LDA	154.25	60.32	75.62	91.63	62.47	152.71	0.22	1.47	-15.30
Ge_1Si_7	LDA	154.38	62.94	75.01	93.42	61.50	151.30	0.23	1.52	-12.07
Ge_1Si_3	LDA	150.33	61.79	72.92	91.30	59.69	147.03	0.23	1.53	-11.13
Ge_3Si_5	LDA	142.36	60.62	71.02	87.87	56.90	140.39	0.23	1.54	-10.40
Ge_1Si_1	LDA	138.22	53.18	70.88	81.53	57.74	140.14	0.21	1.41	-17.70
Ge_5Si_3	LDA	133.47	46.38	68.83	75.41	57.29	137.13	0.20	1.32	-22.45
Ge_3Si_1	LDA	127.70	49.75	65.93	75.73	53.40	129.70	0.21	1.42	-16.18
Ge_7Si_1	LDA	122.23	48.18	64.04	72.86	51.40	124.85	0.21	1.42	-15.86
Ge	LDA	119.57	46.98	62.17	71.18	50.10	121.73	0.21	1.42	-15.19
Si	PBE	158.20	63.56	76.83	95.11	63.26	155.34	0.23	1.50	-13.27
Ge_1Si_7	PBE	153.98	62.13	74.75	92.75	61.48	151.07	0.23	1.51	-12.62
Ge_1Si_3	PBE	150.33	61.79	72.92	91.30	59.69	147.03	0.23	1.53	-11.13
Ge_3Si_5	PBE	145.84	66.22	70.11	92.76	55.87	139.58	0.25	1.66	-3.89
Ge_1Si_1	PBE	141.77	58.14	71.10	86.02	57.46	140.99	0.23	1.50	-12.96
Ge_5Si_3	PBE	137.07	50.63	69.48	79.44	57.44	138.85	0.21	1.38	-18.85
Ge_3Si_1	PBE	131.36	55.37	65.25	80.70	52.52	129.48	0.23	1.54	-9.88
Ge_7Si_1	PBE	125.86	54.05	63.61	77.99	50.57	124.74	0.23	1.54	-9.56
Ge	PBE	120.66	52.89	61.34	75.48	48.34	119.51	0.24	1.56	-8.45

features. Based on these calculated elastic constants, the bulk modulus (B), shear modulus (G), Young's modulus (E), Poisson's ratio (υ) and Pugh's ratio (P) were determined with the Voigt-Reuss-Hill approximations[121-123].

The bulk modulus (B) is defined as the ratio of the infinitesimal pressure increase to the corresponding decrease in volume. Similarly, with C_{11} elastic constant, greater bulk modulus means less volume change under the same external compression. Besides, the shear modulus has a positive correlation with C_{44}, which determines the hardness of the

material. Young's modules can predict the stiffness of the material, and it is evident that Si-like alloys are stiffer than Ge-like alloys.

The brittle nature of the GeSi alloy system can be estimated by several values. Firstly, Frantsevich rule limits a Poisson's ratio of 0.26 as the border between ductile and brittle manners[124]; when Poisson's ratio is greater than 0.26, the material exhibits ductile nature and vice versa. The greatest Poisson's ratio in this study is 0.249, which is still less than the critical value of 0.26, which improves the GeSi alloy system’s brittle performance. Secondly, negative Cauchy pressure means that the material has brittle nature and covalent bonding, rather than ductile manner and ionic bonding[125]. All the Cauchy pressures of the whole series are less than zero. Thirdly, Just like Poisson's ratio, the Pugh ratio also has a critical value of 1.75; where the brittle nature has a value less than 1.75, while Pugh's ratio of material with ductile nature is always greater than 1.75. [126] GeSi alloys’ Pugh’s ratios fall within the range of 1.31~1.66[127].

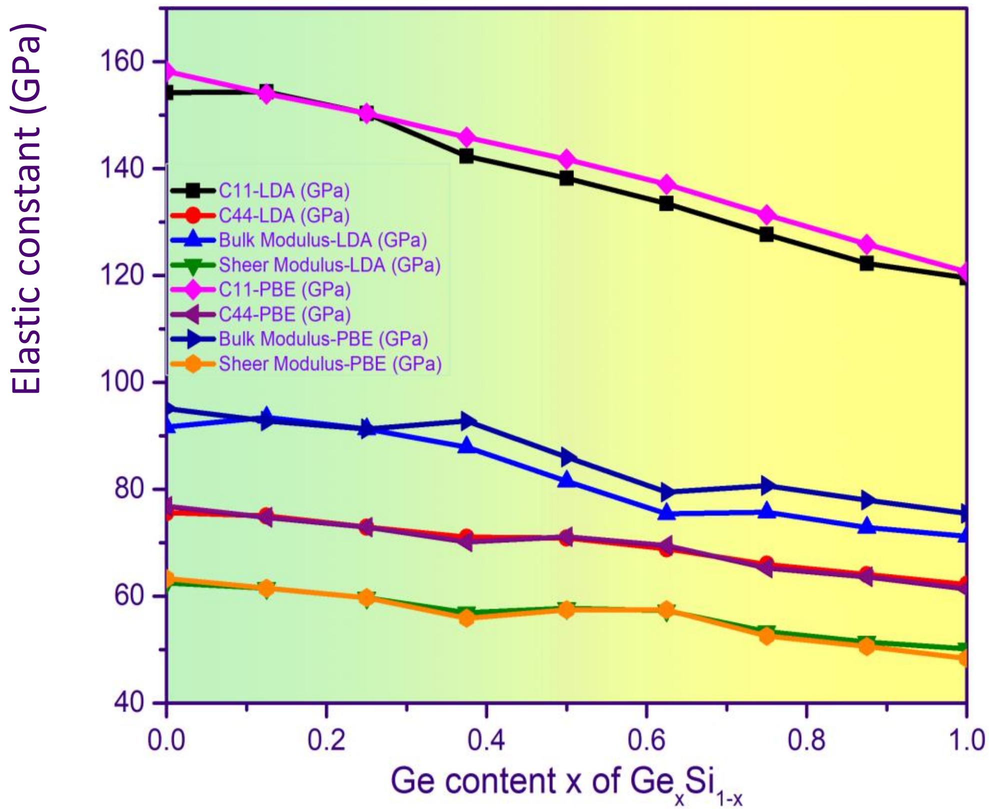

Figure 4-2 Elastic properties of Ge_xSi_{1-x} alloys

4.2 Electronic properties

4.2.1 Band gap

The band gap is a significant factor in determining the electrical conductivity of the material, especially for solid semiconductors. In this work, several GeSi alloy models with different Ge contents were selected, and their bandgap properties were calculated within VASP. Different exchange-correlation functionals, LDA, GGA-PBE and HSE06, and the results are plotted in Figure 4-3.

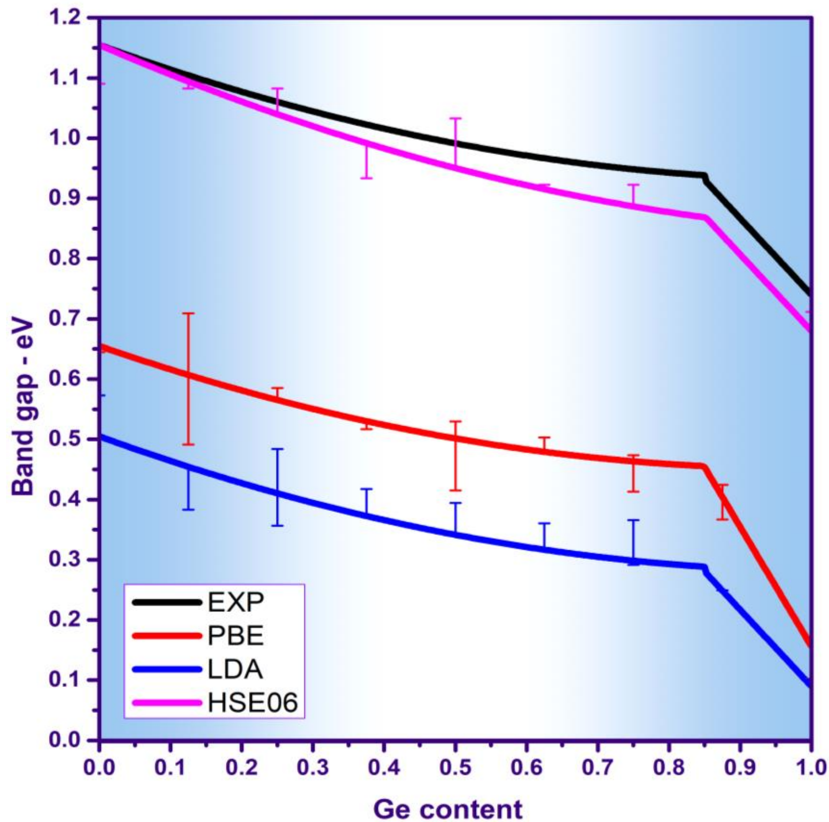

Figure 4-3 Ge_xSi_{1-x} band gap calculated by different functionals

The experimental value shows that the band gap value of GeSi alloy has a strong correlation with Ge/Si ratio. When the Ge content x infinitely closes to zero, the alloy's band gap value almost equal to pure Si and vice versa. This trend has been published in previous experiment studies[10]. The interesting thing is, no matter which functional is used and whether the band gap is underestimated or not, there is always an inflection point at around a Ge content for x=0.85. Below a Ge content of 0.85, the band gap value decreases slowly with increasing Ge content; for higher Ge content, the band gap value

decreases dramatically, until it becomes close to the pure Ge experimental value. One possible explanation for this phenomenon is that the Si-Si bonding predominates at in the Ge concentration range (0-0.85) which forces the GeSi alloy to remain in the Si-based crystal structure but with observable strain. At higher Ge concentrations, the crystal structure reaches to a critical point where the strain cannot maintain that structure, and instead becomes Ge-like. The band gap value begins to resemble pure Ge. Another possible explanation is that the slowly decreasing band gap before the inflexion point refers to Si-like *X*-conduction-band minimum, whereas the rapidly decreasing band gap with Ge content refers to Ge-like *L*-conduction-band minimum.

It is a common issue that LDA and GGA-PBE can numerically underestimate the band gap values, and it is proved in this study.[128] By observation, GGA-PBE underestimates the experimental band gap by around 0.5eV for Si-like alloys, with this underestimated value decreasing with increasing Ge content. In Ge-like alloys, PBE calculated a band gap around 0.4eV less than experimental band gap value. For LDA, its underestimation is greater than PBE results.

However, HSE06 results are in good agreement with the experimental data. At the pure Si point, the HSE06 method agrees with the experimental band gap. The difference between the HSE06 l and experimental values increases gradually, from 0eV to about 0.06eV at Ge-like side. In order to prove/validate this viewpoint, the similar band gap calculation method was applied on III-V semiconductors. The band structures of ternary alloys $In_xGa_{1-x}As$ and $Al_xGa_{1-x}As$ was calculated by PBE, LDA and HSE06 methods, and the results shown in Figure 4-4 and Figure 4-5. It shows that the situation is highly similar to that of Ge_xSi_{1-x}.

For $In_xGa_{1-x}As$, the band gap curve is smooth monotonically decreasing with the increase in alloy content because both GaAs and InAs are materials with direct band gaps, and for both, the lowest point of the conduction band and the highest point of the valence band are in the Γ direction, which means that even with the increase of InAs in the ternary alloy, the valley which the lowest band gap occurs of the alloy remains. In the curve of $In_xGa_{1-x}As$, PBE and LDA still underestimate the actual band gap value, which are 30% to 40% of the theoretical band gap value, while the result of LDA is still lower than that of PBE. The results of HSE06 are still in good agreement with the theoretical values and

slightly lower than the theoretical values in the region of x<0. 75. It underestimates the GaAs about 0.1eV and overestimates the InAs about 0.1eV, which leads to the crossover

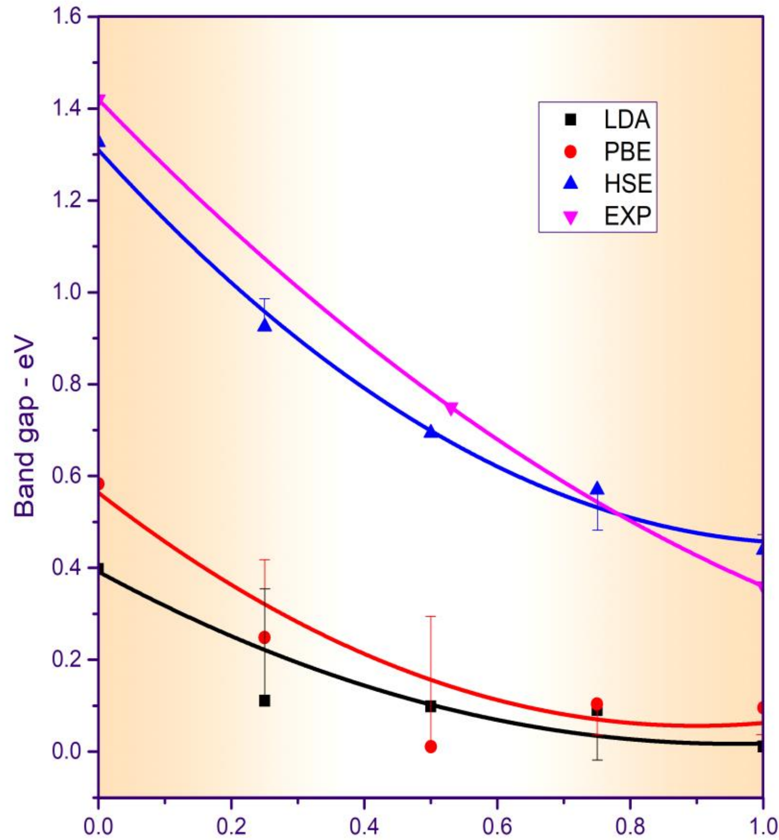

Figure 4-4 $In_xGa_{1-x}As$'s band gap calculated by different functionals

of the HSE06 results and the theoretical values.

For $Al_xGa_{1-x}As$, its band gap has an inflection point at about x = 0.4, because the direct energy gap of GaAs is in the Γ direction, while that of InAs is an indirect one, for which the valence band top is in Γ direction, but the bottom of the conduction band is in X valley. This inflection point is the intersection of the X-G band gap curve and the G-G band gap curve. Similarly, the results show that PBE and LDA underestimate the band gap value, which is about 30% to 46% of the theoretical value, and the result of PBE is higher than that of LDA. HSE06 underestimates GaAs by 0.1eV, by underestimating AlAs by about 0.17eV, so the gap between the linear trend line of HSE06 results and that of theoretical values gradually increases from x=0 to x=1, but the error never exceeded

4.5%. Therefore, compared with PBE and LDA, the HSE06 calculations are in good agreement with the experimental band gap values.

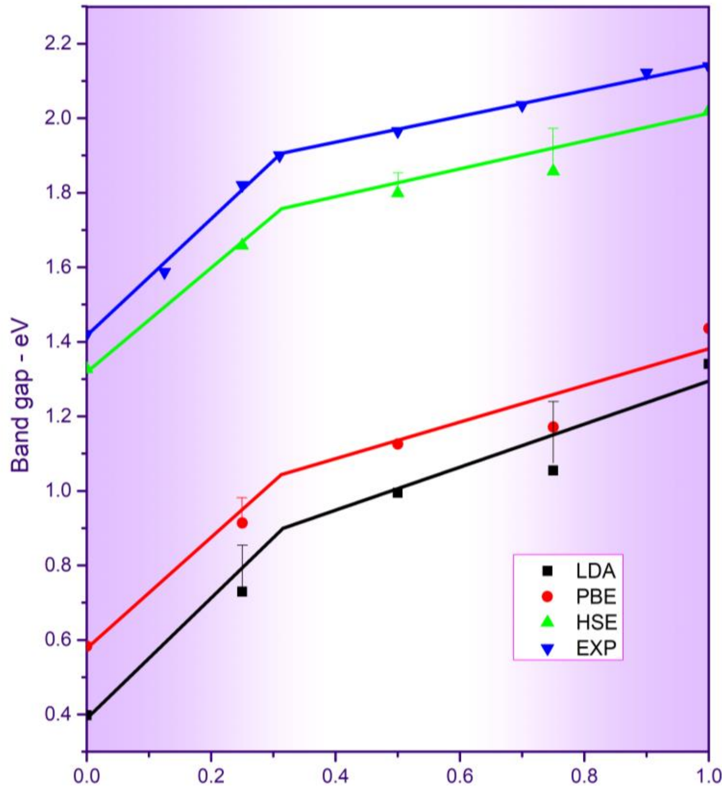

Figure 4-5 $Al_xGa_{1-x}As$'s band gap calculated by different functionals

It is well known that the non-local Fock (exact) exchange energy in the Hartree-Fock method is not a density functional, it cancels the pseudo-self-interaction but does not include contributions from the electronic correlation. Therefore, the exchange is long range and not screened, the excitation energy is unrealistically high, and the band gap tends to be highly overestimated[129]. Considering that HF method overestimates band gap while LDA (or GGA) underestimates it, some hybrid exchange-correlation functionals that combine HF and LDA (or GGA) functionals have been investigated to achieve a proper intermediate result, and HSE06 is one of them. By adjusting screening and mix parameter, HSE06 calculations of GeSi alloy system band gap values are close to that of the experimental band gap. Therefore, HSE06 performs much better.

4.2.2 DOS and charge density

PDOS and band graphs are indispensable to investigate the whole system's electronic property. Ge_1Si_7 has been selected as a representative concentration, with its pDOS band structure graphs with high symmetry directions *L, Γ, X* shown in Figure 4-6. Considering

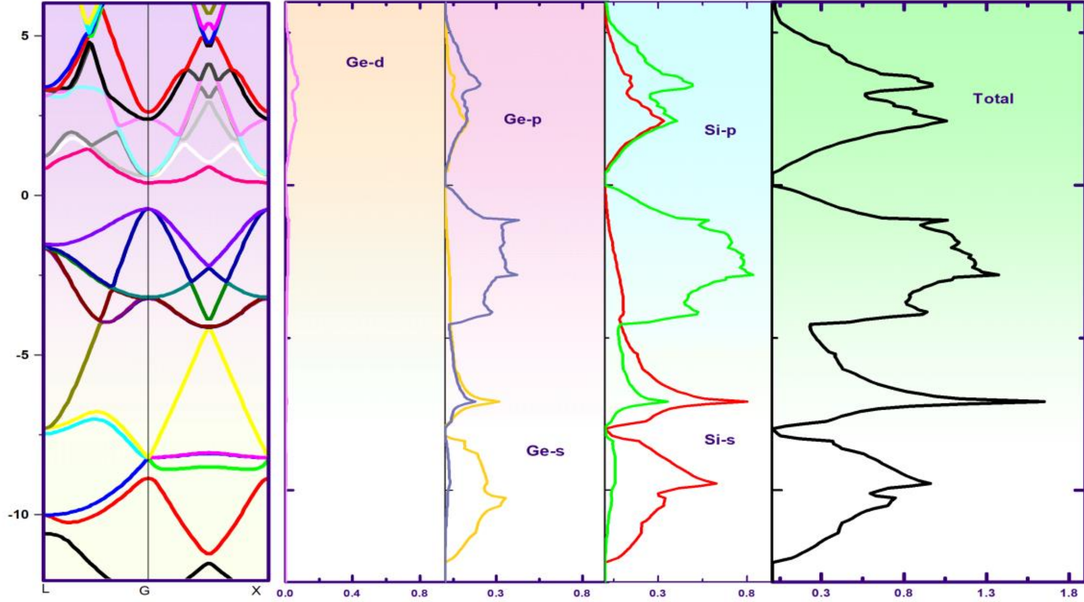

Figure 4-6 Band structure and pDOS of Ge_1Si_7

computing efficiency, this figure was calculated by LDA. It can be noticed that the gap between conduction band bottom and valence band top is larger than the DOS gap at 0eV, this is because GeSi is a semiconductor with an indirect band, the band gap in the *Γ* direction is not the minimum. It is obvious that DOS graph consists of 3 parts, and most states occur between -12.5eV to 6eV. Ge and Si's *p* orbitals occupy the major component from -12.5eV to -7eV, and density of Si-*p* state is larger than Ge-*p* state's density. In energy area from -7eV to 0eV, *s* orbitals of both Ge and Si contributes the most for total DOS, and Ge *s* density is still around twice that of Si *s*. The density of Ge-*d* state is the weakest component; its high area is from 0eV to 6eV, where it is half strong as Ge-*p* density of state.

To better understand the interaction among atoms in GeSi, 2D contour maps Figure 4-8 and 3D isosurface graph Figure 4-7 were computed, two 2D graphs Figure 4-8a and Figure 4-8b are along (011) plane of Ge_1Si_1 and (111) plane of Ge_3Si_5, respectively. No matter whether it is Ge-Si or Si-Si bonding, charge between them is shared, which indicates the covalence bonding nature of both Ge-Si and Si-Si. Since Ge has a greater attraction for electrons than Si, and that Ge is around 4% greater in size than Si (shape of orbitals), the Ge-Si covalent bond is polar. Charge density 3D isosurface graph of Ge_4Si_4

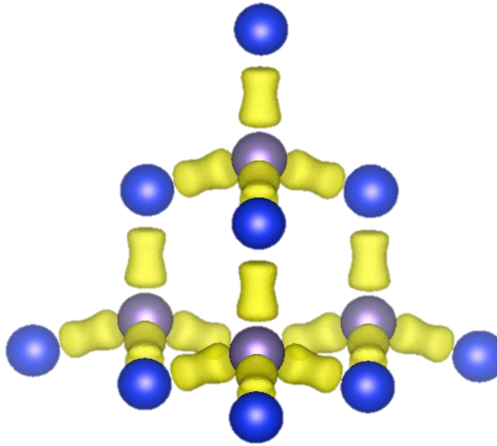

Figure 4-7 Charge density 3D isosurface graph of Ge_4Si_4

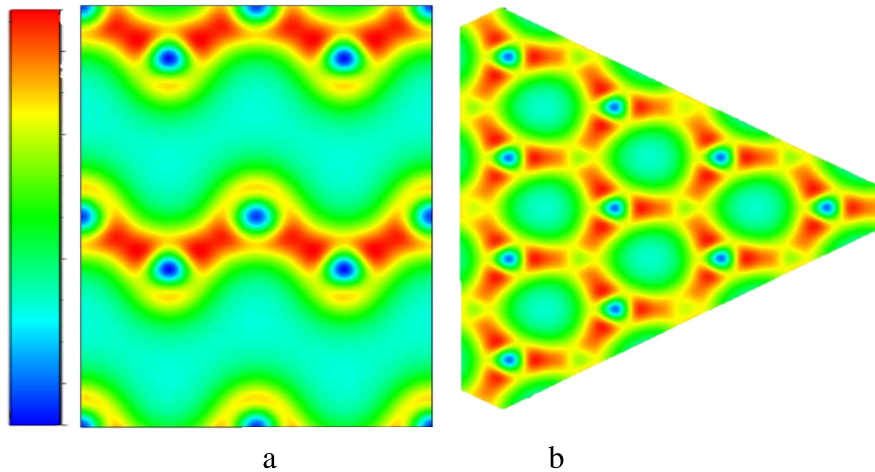

Figure 4-8 Charge density 2D contour maps of Ge_4Si_4 along (011) plane (a) and Ge_3Si_5 along (111) plane (b)

5 Summary and future work

5.1 Conclusion

In this work, a systematic *ab-initio* investigation of structural, elastic and electronic properties of Ge_xSi_{1-x} alloy has been performed. Based on Vegard's Law, Ge_xSi_{1-x} alloys' structural models with certain Ge contents were generated by modification from existent similar structures. Calculations using VASP and analysing the results, their hardness, stiffness, brittleness, band gap width, DOS orbital contribution and bonding nature were calculated and discussed.

Previous work using LDA and GGA-PBE method to calculate alloy band gap width are commonly inaccurate. In this study, the HSE06 hybrid functional was used to calculate Ge_xSi_{1-x} alloy's band gap width, the results show that this method gives much more accurate outcome than LDA and GGA-PBE. The method is also applied in other material systems, $In_xGa_{1-x}As$ and $Al_xGa_{1-x}As$, for comparison. It was found that the band gap calculated using the HSE06 potential is in good agreement with the experimental values compared with LDA and GGA-PBE. This means that the material band properties predicted calculate with HSE06 hybrid functional are more meaningful for reference, which provides for a better predictor of the material band gap for materials systems that can be used to synthesize new materials with tuned band gap. This will be more important in those materials where composite systems are desired.

5.2 Limitation

Although Ge_xSi_{1-x} materials have excellent properties including high carrier mobility, tuneable band gap, they also have shortcomings. Because the lattice constant of Ge is 4.2% larger than that of Si, the inside strain energy is formed, which significantly affects the band gap and structural, and electrical properties of the material. In this work, only the ideal alloy structures are calculated, and the possible effects of strain were not considered. In order to make the results more reliable, the crystal structure modelling method should be improved taking strain effects into account. One method is to form superlattices that can more accurately represent the crystal structure of these alloys. However, this comes at a cost, as these superstructures are large, so that significantly

more computing power is required and hence calculation times become horrendous. A second method, possibly more computational expensive would be to model potential systems including dislocations and strain.

5.3 Future work

Ge_xSi_{1-x} alloy systems offer potential for TE materials, and theoretically investigating and improving its TE property could be a promising research direction. It is entirely possible to indirectly adjust its TE properties, such as electrical and thermal conductivity, employing energy band engineering. The promise of effective adjustment is to accurately and quantitatively predict the thermal and electrical conductivity of materials with certain band nature.

VASP itself doesn't carry any available code that can calculate TE properties. Therefore, in the future, BoltzTraP code[130] could be applied on TE property calculations. Under the constant relaxation time approximation, BoltzTraP can solve the semiclassical Boltzmann transport equation.[131] Based on that, Ge_xSi_{1-x} alloys' TE properties will be calculated at low, mid, and high temperature area, which includes Seebeck coefficient S, electric conductivity σ, thermal conductivity K, and power factor σS^2. Finally, their ZT values at different temperatures will be inferred, combined with their band information, the connection between them can be revealed. The band gap with the best ZT value could be an excellent guide for further experiment.

6 Bibliography

1. *Global Energy Statistical Yearbook.* Enerdata;2017.
2. *State of the energy market.* Australian Energy Regulator;2018.
3. Statistics ABo. Energy Use, *Electricity Generation and Environmental Management, Australia, 2014-15*;2016.
4. Goel PK. *Water Pollution: Causes, Effects and Control.* New Age International Publishers; 2011.
5. Sootsman JR, Chung DY, Kanatzidis MG. New and Old Concepts in Thermoelectric Materials. 2009;48(46):8616-8639.
6. Dismukes JP, Ekstrom L, Paff RJ. Lattice Parameter and Density in Germanium-Silicon Alloys. *The Journal of Physical Chemistry.* 1964;68(10):3021-3027.
7. Lange RG, Carroll WP. Review of recent advances of radioisotope power systems. 2008;49(3):393-401.
8. Ashburn P. *SiGe Heterojunction Bipolar Transistors.* 2004.
9. Li T, Fang F, Yang Y, et al. Surface nano-engineered wheat straw for portable and adjustable water purification. *Sci Total Environ.* 2019;655:1028-1036.
10. Weber J, Alonso MI. Near-band-gap photoluminescence of Si-Ge alloys. *Physical Review B.* 1989;40(8):5683-5693.
11. Cappellini G, Satta G, Palummo M, Onida G. Electronic and Optical Properties of SiGe alloys within first-principles schemes. 2004;829.
12. Moontragoon P. *Calculation of Electronic Structure and Thermoelectric Properties of Ge(1-x)Six Alloy.* Vol 402013.
13. Zellat K, Soudini B, Sekkal N, Ait Cheikh S. *Computational Investigation of Electronic and Optical Properties of Si, Ge and Si1-xGex Alloys Using the FP-LMTO Method Augmented by a Plane-Wave Basis.* Vol 22012.
14. Kohn W, Sham LJ. Self-Consistent Equations Including Exchange and Correlation Effects. *Physical Review.* 1965;140(4A):A1133-A1138.
15. Kohn W, Becke AD, Parr RG. Density Functional Theory of Electronic Structure. *The Journal of Physical Chemistry.* 1996;100(31):12974-12980.
16. Perdew JP, Burke K, Ernzerhof M. Generalized Gradient Approximation Made Simple. *Physical Review Letters.* 1996;77(18):3865-3868.
17. Kresse G, Furthmüller J. Efficiency of ab-initio total energy calculations for metals and semiconductors using a plane-wave basis set. *Computational Materials Science.* 1996;6(1):15-50.
18. Kresse G, Furthmüller J. Efficient iterative schemes forab initiototal-energy calculations using a plane-wave basis set. *Physical Review B.* 1996;54(16):11169-11186.
19. Rowe DM. *Modern thermoelectrics.* London: Holt, Rinehart and Winston; 1983.
20. A.V. Ioffe AFI, Dokl. Akad. *Nauk SSSR* 1954;97:821.
21. Klemens PG. Thermal Resistance due to Isotopic Mass Variation. *Proceedings of the Physical Society Section A.* 1957;70(11):833-836.
22. Goldsmid HJ. *Introduction to Thermoelectricity.* Berlin, Heidelberg: Springer; 2016.

23. Steele MC, Rosi FD. Thermal Conductivity and Thermoelectric Power of Germanium‐Silicon Alloys. *Journal of Applied Physics.* 1958;29(11):1517-1520.
24. Slack GA, Hussain MA. The Maximum Possible Conversion Efficiency of Silicon-Germanium Thermoelectric Generators. *Journal of Applied Physics.* 1991;70(5):2694-2718.
25. Slack DS, Patrick RE, Miller JR. Fenix, a Test Facility for Iter and Other New Superconducting Magnets. *Ieee T Magn.* 1991;27(2):1835-1838.
26. Poudel B, Hao Q, Ma Y, et al. High-thermoelectric performance of nanostructured bismuth antimony telluride bulk alloys. *Science.* 2008;320(5876):634-638.
27. Wang XW, Lee H, Lan YC, et al. Enhanced thermoelectric figure of merit in nanostructured n -type silicon germanium bulk alloy. *Applied Physics Letters.* 2008;93(19).
28. Joshi G, Lee H, Lan Y, et al. Enhanced thermoelectric figure-of-merit in nanostructured p-type silicon germanium bulk alloys. *Nano Lett.* 2008;8(12):4670-4674.
29. Mingo N, Hauser D, Kobayashi NP, Plissonnier M, Shakouri A. "Nanoparticle-in-alloy" approach to efficient thermoelectrics: silicides in SiGe. *Nano Lett.* 2009;9(2):711-715.
30. Bera C, Soulier M, Navone C, et al. Thermoelectric properties of nanostructured Si1-xGex and potential for further improvement. *J Appl Phys.* 2010;108(12).
31. He Y, Donadio D, Galli G. Morphology and Temperature Dependence of the Thermal Conductivity of Nanoporous SiGe. *Nano Letters.* 2011;11(9):3608-3611.
32. Vining CB. A Model for the High-Temperature Transport-Properties of Heavily Doped N-Type Silicon-Germanium Alloys. *J Appl Phys.* 1991;69(1):331-341.
33. Zhu GH, Lee H, Lan YC, et al. Increased phonon scattering by nanograins and point defects in nanostructured silicon with a low concentration of germanium. *Phys Rev Lett.* 2009;102(19):196803.
34. Shi LH, Yao DL, Zhang G, Li BW. Large thermoelectric figure of merit in Si1-xGex nanowires. *Appl Phys Lett.* 2010;96(17).
35. Mishima Y, Kimura Y, Wng Kim S. CHAPTER 11 - Enhancement of Thermoelectric Figure of Merit through Nanostructural Control on Intermetallic Semiconductors toward High-Temperature Applications. In: Hosono H, Mishima Y, Takezoe H, et al., eds. *Nanomaterials.* Oxford: Elsevier Science Ltd; 2006:383-418.
36. Seebeck TJ, Oettingen Av. *Magnetische polarisation der metalle und erze durch temperatur-differenz.* Leipzig,: W. Engelmann; 1825.
37. Peltier. *Annales de Chimie et de Physique.* Vol 561834.
38. Thomson W. *R. Soc. Edinburgh: Earth Sci. 3.* Thomson Biography; 1851.
39. Riksanagara R. Design and Implementation of Thermoelectric Module On Fire Charging System For Customers Ascent. *Journal, Telkom University, Bandung.* 2012.
40. Venkateshvaran D, Kronemeijer AJ, Moriarty J, Emin D, Sirringhaus H. Field-effect modulated Seebeck coefficient measurements in an organic polymer using a microfabricated on-chip architecture. *APL Materials.* 2014;2(3):032102.
41. Snyder GJ. *Thermoelectrics Handbook: Macro to Nano.* CRC Press; 2009.

42. Hicks LD, Dresselhaus MS. Effect of quantum-well structures on the thermoelectric figure of merit. *Phys Rev B Condens Matter.* 1993;47(19):12727-12731.
43. Gelbstein Y, Dashevsky Z, Dariel MP. High performance n-type PbTe-based materials for thermoelectric applications. *Physica B.* 2005;363(1-4):196-205.
44. Dmitriev AV, Zvyagin IP. Current trends in the physics of thermoelectric materials. *Physics-Uspekhi.* 2010;53(8):789-803.
45. Chen Z-G, Han G, Yang L, Cheng L, Zou J. Nanostructured thermoelectric materials: Current research and future challenge. 2012;22(6):535-549.
46. Mao J, Liu Z, Ren Z. Size effect in thermoelectric materials. 2016;1:16028.
47. Szczech JR, Higgins JM, Jin S. Enhancement of the thermoelectric properties in nanoscale and nanostructured materials. 2011;21(12):4037-4055.
48. Bell LE. Cooling, heating, generating power, and recovering waste heat with thermoelectric systems. *Science.* 2008;321(5895):1457-1461.
49. Xie W, Weidenkaff A, Tang X, Zhang Q, Poon J, Tritt T. Recent Advances in Nanostructured Thermoelectric Half-Heusler Compounds. 2012;2(4):379-412.
50. Graf T, Felser C, Parkin S. *Simple rules for the understanding of Heusler compounds.* Vol 392011.
51. Harame DL, Koester SJ, Freeman G, et al. The revolution in SiGe: impact on device electronics. 2004;224(1-4):9-17.
52. li H, Tang X, Zhang Q, Uher C. *High performance InxCeyCo4Sb12 thermoelectric materials with in situ forming nanostructured InSb phase.* Vol 942009.
53. Huang D. A Nanocomposite Approach: Lowering Thermal Conductivity of Si-Ge Thermoelectric Materials for Power Generation Applications. *Journal of Applied Mechanical Engineering.* 2014.
54. Mahan GD. Good Thermoelectrics. In: Ehrenreich H, Spaepen F, eds. *Solid State Physics.* Vol 51. Academic Press; 1998:81-157.
55. Xun Shi LX, Jiong Yang, Wenqing Zhang, Lidong Chen. Basic physics in thermoelectrics. *Physics.* 2011;40(11).
56. He R, Schierning G, Nielsch K. Thermoelectric Devices: A Review of Devices, Architectures, and Contact Optimization. *Advanced Materials Technologies.* 2017:1700256.
57. Yang JH, Caillat T. Thermoelectric materials for space and automotive power generation. *Mrs Bull.* 2006;31(3):224-229.
58. L. Rebenklau PG, A. Paproth, K. Irrgang, L. Lippmann,. A. Wodtke, L. Niedermeyer, K. Augsburg, F. Bechtold. Paper presented at: 2015 European Microelectronics Packaging Conf. (Empc)2015; Friedrichshafen, Germany.
59. Finney FT, McPheters A, Singer NV, et al. Microvasculature of the Plantar Plate Using Nano-Computed Tomography. *Foot Ankle Int.* 2019;40(4):457-464.
60. Champier D. Thermoelectric generators: A review of applications. *Energy Conversion and Management.* 2017;140:167-181.
61. Bennett GL. Space Nuclear Power: Opening the Final Frontier. 4th International Energy Conversion Engineering Conference and Exhibit; 2006.

62. Taylor RA, Solbrekken GL. Comprehensive system-level optimization of thermoelectric devices for electronic cooling applications. *IEEE Transactions on Components and Packaging Technologies.* 2008;31(1):23-31.
63. LeBlanc S, Yee SK, Scullin ML, Dames C, Goodson KE. Material and manufacturing cost considerations for thermoelectrics. *Renewable and Sustainable Energy Reviews.* 2014;32(C):313-327.
64. Committee ASMIH. *ASM handbook.* Materials Park, Ohio: ASM International; 1990.
65. Algarra M, Bartolic D, Radotic K, et al. P-doped carbon nano-powders for fingerprint imaging. *Talanta.* 2019;194:150-157.
66. Montgomery R, McDowall R. Chapter 5 - Self- and System-powered Controls. In: Montgomery R, McDowall R, eds. *Fundamentals of HVAC Control Systems.* Oxford: Elsevier; 2008:160-166.
67. Meseguer J, Pérez-Grande I, Sanz-Andrés A. 15 - Thermoelectric cooling. In: Meseguer J, Pérez-Grande I, Sanz-Andrés A, eds. *Spacecraft Thermal Control.* Woodhead Publishing; 2012:263-273.
68. Lv M. *COMPUTER SIMULATION ON STRUCTURES AND ELECTRONIC PROPERTIES OF SILICON AND GERMANIUM AND THEIR ALLOYS* Yanshan University 2005.
69. Yonenaga I. Czochralski growth of GeSi bulk alloy crystals. 1999;198-199:404-408.
70. Wollweber J, Schulz D, Schröder W. Extremely reduced dislocation density in SixGe1 − x single crystals grown by the float zone technique. *Journal of Crystal Growth.* 1996;158(1-2):166-168.
71. Bridgman PW. The Compressibility of Thirty Metals as a Function of Pressure and Temperature. *Proceedings of the American Academy of Arts and Sciences.* 1923;58(5):165-242.
72. Dahlen A, Fattah A, Hanke G, Karthaus E. Bridgman and Czochralski growth of Ge Si alloy crystals. *Crystal Research and Technology.* 1994;29(2):187-198.
73. Kadokura K, Takano Y. Germanium-silicon single crystal growth using an encapsulant in a silica ampoule. *Journal of Crystal Growth.* 1997;171(1):56-60.
74. Zhang J, Lees AK, Taylor AG, et al. In-situ monitoring of Si and SiGe growth on Si(001) surfaces during gas-source molecular beam epitaxy using reflectance anisotropy. 1996;164(1-4):40-46.
75. Arimoto K, Nakazawa H, Mitsui S, et al. Growth of strained Si/relaxed SiGe heterostructures on Si(110) substrates using solid-source molecular beam epitaxy. *Semiconductor Science and Technology.* 2017;32(11):114002.
76. Hartmann JM, Loup V, Rolland G, et al. SiGe growth kinetics and doping in reduced pressure-chemical vapor deposition. *Journal of Crystal Growth.* 2002;236(1):10-20.
77. Boer WBD, Theunissen MJJ, Linden RHJVD. The Necessity of RTCVD in Advanced Epitaxial Growth of Si and SiGe. *MRS Proceedings.* 1995;387:287.
78. Schaeffer DA. *Fabrication and Characterization of Si(1-x)Ge(x) Semiconductor Alloy for Sensor Applications*, University of Tennessee; 2013.
79. Deng X. *Handbook of Photovoltaic Science and Engineering.* 2003.

80. Leblanc S. Thermoelectric generators: Linking material properties and systems engineering for waste heat recovery applications. *Sustainable Materials and Technologies.* 2014;1-2:26-35.
81. Esaki L, Tsu R. Superlattice and Negative Differential Conductivity in Semiconductors. *IBM Journal of Research and Development.* 1970;14(1):61-65.
82. Pearsall TP, Vandenberg JM, Hull R, Bonar JM. Structure and optical properties of strained Ge-Si superlattices grown on (001) Ge. *Physical Review Letters.* 1989;63(19):2104-2107.
83. Perera AGU. Chapter 5 - Semiconductor Photoemissive Structures for Far Infrared Detection. In: Francombe MH, ed. *Handbook of Thin Film Devices.* Burlington: Academic Press; 2000:135-170.
84. Terasaki I. Thermal Conductivity and Thermoelectric Power of Semiconductors. In: *Reference Module in Materials Science and Materials Engineering*. Elsevier; 2016.
85. Bulusu A, Walker DG. Review of electronic transport models for thermoelectric materials. *Superlattice Microst.* 2008;44(1).
86. Space Radioisotope Power Systems Multi-Mission Radioisotope Thermoelectric Generator. NASA. Published 2013. Accessed.
87. Lombardo GLBaJJ. Mission of Daring: The General-Purpose Heat Source Radioisotope Thermoelectric Generator. 4th International Energy Conversion Engineering Conference and Exhibit (IECEC); 26-29 June, 2006; San Diego, California.
88. Cassini Spacecraft Arrives at Saturn. https://www.nasa.gov/mission_pages/cassini/media/cassini-063004-soi.html. Published 2004. Accessed.
89. Chen C, Cai L, Shangguan X, Li L, Hong Y, Wu G. Heterogeneous and efficient transesterification of Jatropha curcas L. seed oil to produce biodiesel catalysed by nano-sized SO4 (2-)/TiO2. *R Soc Open Sci.* 2018;5(11):181331.
90. Ulysses Spacecraft Ends Historic Mission of Discovery. NASA. https://www.jpl.nasa.gov/news/news.php?release=2009-104. Published 2009. Accessed.
91. Ulysses: 12 extra months of valuable science. European Space Agency. Published 2009. Accessed.
92. Kroemer H. Theory of a Wide-Gap Emitter for Transistors. *Proceedings of the IRE.* 1957;45(11):1535-1537.
93. Chang MF, Asbeck PM, Wang KC, et al. Heterojunction bipolar transistor technology for analog and digital applications. Paper presented at: International Electron Devices and Materials Symposium; 12-15 July 1994, 1994.
94. Asbeck PM, Chang MF, Wang KC, Sullivan GJ. Chapter 4 - Heterojunction Bipolar Transistors in III—V Semiconductors. In: Einspruch NG, Frensley WR, eds. *VLSI Electronics Microstructure Science.* Vol 24. Elsevier; 1994:107-155.
95. Cressler JD, Hamilton MC, Krithivasan R, et al. Proton radiation response of SiGe HBT analog and RF circuits and passives. *IEEE Transactions on Nuclear Science*. 2001;48(6):2238-2243.
96. G.Niu JDCa. *Silicon-Germanium Heterojunction Bipolar Transistors.* Boston, MA: Artech House; 2003.

97. Nixdorff K, Borisova T, Komisarenko S, Dando M. Dual-Use Nano-Neurotechnology: An assessment of the implications of trends in science and technology. *Politics Life Sci.* 2018;37(2):180-202.
98. Chen B. *RFIC applications with CMOS technology* [Ph.D.]. Ann Arbor, City University of New York; 2006.
99. Hong Fan X, Xu B, Xu Y, et al. Application of Materials Studio Modeling in Crystal Structure. *Advanced Materials Research.* Vol 706-7082013.
100. BIOVIA. Materials Studio Overview. BIOVIA. http://accelrys.com/products/collaborative-science/biovia-materials-studio/. Accessed.
101. Vegard L. Die Konstitution der Mischkristalle und die Raumfüllung der Atome. 1921;5(1):17-26.
102. Wyckoff. R. W. G. In. Vol Second Edition: Interscience Publishers, New York; 1963:783.
103. Kresse G, Joubert D. From ultrasoft pseudopotentials to the projector augmented-wave method. *Physical Review B.* 1999;59(3):1758-1775.
104. Kresse G, Hafner J. Norm-conserving and ultrasoft pseudopotentials for first-row and transition elements. *Journal of Physics: Condensed Matter.* 1994;6(40):8245-8257.
105. Born M, Oppenheimer R. Quantum theory of molecules. *Ann Phys-Berlin.* 1927;84(20):0457-0484.
106. Kohn W, Sham LJ. Self-Consistent Equations Including Exchange and Correlation Effects. *Phys Rev.* 1965;140(4a):1133-&.
107. Ylvisaker ER. *DFT and DMFT: Implementations and applications to the study of correlated materials* [Ph.D.]. Ann Arbor, University of California, Davis; 2008.
108. Schwarz K. DFT calculations of solids with LAPW and WIEN2k. *J Solid State Chem.* 2003;176(2):319-328.
109. Cancès E. Self-consistent field algorithms for Kohn–Sham models with fractional occupation numbers. *The Journal of Chemical Physics.* 2001;114(24):10616-10622.
110. Fermi E. *Un Metodo Statistico per la Determinazione di alcune Prioprietà dell'Atomo.* Vol 6: Rendiconti Academia Dei Lincei; 1927.
111. Thomas LH. The calculation of atomic fields. *Mathematical Proceedings of the Cambridge Philosophical Society.* 1927;23(5):542-548.
112. Scanlon DO, Walsh A. Bandgap engineering of ZnSnP2 for high-efficiency solar cells. *Applied Physics Letters.* 2012;100(25):251911.
113. Janesko BG, Henderson TM, Scuseria GE. Screened hybrid density functionals for solid-state chemistry and physics. *Physical Chemistry Chemical Physics.* 2009;11(3):443-454.
114. Yang S, Olishevski P, Kertesz M. Bandgap calculations for conjugated polymers. *Synthetic Metals.* 2004;141(1):171-177.
115. Zhuang HL, Hennig RG. Electronic structures of single-layer boron pnictides. *Applied Physics Letters.* 2012;101(15):153109.
116. Heyd J, Scuseria GE, Ernzerhof M. Hybrid functionals based on a screened Coulomb potential. *J Chem Phys.* 2003;118(18):8207-8215.

117. Fu CL, Ho KM. First-principles calculation of the equilibrium ground-state properties of transition metals: Applications to Nb and Mo. *Physical Review B.* 1983;28(10):5480-5486.
118. Born M, Huang K. *Dynamical theory of crystal lattices.* Oxford : Clarendon Press; 1954.
119. Hu Q, Wu Q, Ma Y, et al. First-principles studies of structural and electronic properties of hexagonal. *Physical Review B.* 2006;73(21):214116.
120. Nielsen OH, Martin RM. Stresses in semiconductors: Ab initio calculations on Si, Ge, and GaAs. *Physical Review B.* 1985;32(6):3792-3805.
121. Voigt W. Wechselbeziehungen zwischen zwei Tensortripeln. (Elastizität und innere Reibung.). In: Voigt W, ed. *Lehrbuch der Kristallphysik: mit Ausschluß der Kristalloptik.* Wiesbaden: Vieweg+Teubner Verlag; 1966:560-800.
122. Chen H, Yang L. Pressure effect on the structural and elastic property of Hf2InC. *Physica B: Condensed Matter.* 2011;406(23):4489-4493.
123. Sun Z, Music D, Ahuja R, Schneider JM. Ab initiostudy of M2AlN (M = Ti,V,Cr). *Journal of Physics: Condensed Matter.* 2005;17(2):L15-L19.
124. I. N. Frantsevich FFV, and S.A. Bokuta. *,Elastic constants and elastic moduli of metals and insulators, handbook.* Naukova Dumka, Kiev; 1983.
125. Pettifor DG. Theoretical predictions of structure and related properties of intermetallics. *Materials Science and Technology.* 1992;8(4):345-349.
126. Pugh SF. XCII. Relations between the elastic moduli and the plastic properties of polycrystalline pure metals. *The London, Edinburgh, and Dublin Philosophical Magazine and J. Sci.*.1954;45(367):823-843.
127. Bannikov VV, Shein IR, Ivanovskii AL. Elastic properties of antiperovskite-type Ni-rich nitrides MNNi3 (M=Zn, Cd, Mg, Al, Ga, In, Sn, Sb, Pd, Cu, Ag and Pt) as predicted from first-principles calculations. *Physica B, Condensed Matter.* 2010;405(22):4615-4619.
128. Fonseca LRC, Knizhnik AA. First-principles calculation of the TiN effective work function on SiO2 and on HfO2. *Physical Review B.* 2006;74(19):195304.
129. Zolyomi V, Kurti J. First-principles calculations for the electronic band structures of small diameter single-wall carbon nanotubes. *Physical Review B.* 2004;70(8).
130. Madsen GKH, Singh DJ. BoltzTraP. A code for calculating band-structure dependent quantities. *Computer Physics Communications.* 2006;175(1):67-71.
131. Aditya Jayaraman ABK, and Muralikrishna Molli. DFT Study on the Carrier Concentration and Temperature-Dependent Thermoelectric Properties of Antimony Selenide. *Indian Journal of Materials Science.* 2016;2016:7.